Department of Physics and Astronomy

Heidelberg University

Master Thesis in Physics

submitted by

Elinor Kath

born in Stuttgart, Germany

2022

Feasibility of
Single-Atom-Resolved Fluorescence Imaging
# of Freely Propagating ^{39}K Atoms

This Master Thesis has been carried out by Elinor Kath

at the Kirchhoff-Institute of Physics

under the supervision of

Prof. Dr. Markus Oberthaler

Abstract

Feasibility of Single-Atom-Resolved Fluorescence Imaging of Freely Propagating ^{39}K Atoms

This thesis explores the feasibility of fluorescence imaging with single-atom-resolution of freely propagating ^{39}K atoms. An Electron Multiplying Charge Coupled Device camera is used to detect and amplify the faint signal. The average number of photoelectrons created by a single atom is calculated, taking into account factors like the atom's natural scattering rate and dipole radiation pattern, as well as the numerical aperture of the imaging objective and the quantum efficiency of the camera. Technical noise sources of the camera and sources of stray light are investigated and reduced. Single-atom fluorescence signals are simulated, taking into account effects of the atom's diffusive motion and the point spread function of the imaging system. Because the signal of single atoms cannot be distinguished from noise based on the pixel values it produces, different criteria are considered and tested on the simulated atom signals. Expectations from the simulations are compared to experimental data and possible reasons for the differences are discussed. Lastly, we suggest the next steps to improve the experimental results.

Zusammenfassung

Realisierbarkeit von Fluoreszenz-Bildgebung mit Einzelatomauflösung von frei propagierenden ^{39}K-Atomen

Diese Arbeit untersucht die Realisierbarkeit von Fluoreszenz-Bildgebung mit Einzelatomauflösung von frei propagierenden ^{39}K-Atomen. Zur Detektion und Verstärkung der schwachen Signale wird eine Charge Coupled Device Kamera mit Sekundärelektronenvervielfacher verwendet. Die durchschnittliche Anzahl an von einem Atom erzeugten Photoelektronen wird berechnet. Hierbei werden unter anderem die natürliche Streurate der Atome und deren Dipol-Abstrahlungsmuster berücksichtigt, sowie die numerische Apertur des Abbildungssystems und die Quanteneffizienz der Kamera. Die technische Ursachen für Rauschen in der Kamera und Quellen von Streulicht werden untersucht und reduziert. Die Fluoreszenzsignale einzelner Atome werden simuliert, wobei die Diffusionsbewegung der Atome sowie die Punktverteilungsfunktion des Abbildungssystems berücksichtigt werden. Da das Signal einzelner Atome nicht anhand der Pixelwerte von Rauschen unterschieden werden kann werden andere Kriterien entwickelt und an simulierten Signalen getestet. Aus den Simulationen gewonnene Erfahrungen werden mit experimentellen Daten verglichen und mögliche Ursachen für die festgestellten Unterschiede diskutiert. Abschließend empfehlen wir die nächsten Schritte zur Verbesserung der experimentellen Ergebnisse.

Contents

1 Introduction 11

2 Fluorescence Imaging of ^{39}K 13
- 2.1 Properties of ^{39}K 13
  - 2.1.1 Level Structure 13
  - 2.1.2 Feshbach Resonances 14
  - 2.1.3 Imaging Transitions 15
- 2.2 Estimating the Mean Signal per Single Atom 16
  - 2.2.1 Scattering Rate 16
  - 2.2.2 Numerical Aperture and Dipole Radiation Pattern 17
  - 2.2.3 Transmission Through Optical Components 17
  - 2.2.4 Quantum Efficiency 18
  - 2.2.5 Expected Photoelectrons per Atom 18
- 2.3 Estimating the Signal Spread 18
  - 2.3.1 Influence of Initial Thermal Velocity 18
  - 2.3.2 Influence of Doppler Shifts 18
  - 2.3.3 Influence of Diffusive Motion 19
  - 2.3.4 Influence of Point Spread Function 21

3 Detecting Low Photon Signals 23
- 3.1 Charge Coupled Device Sensors 23
- 3.2 Noise Sources of CCD Cameras 23
  - 3.2.1 Thermal Counts 24
  - 3.2.2 Clock-Induced Charges 24
  - 3.2.3 Readout Noise 25
- 3.3 Electron Multiplying CCD Cameras 25
- 3.4 Image Binarization 26

4 Experimental Setup 31
- 4.1 The BECK Experiment 31
- 4.2 Imaging Setup 32
- 4.3 Camera ProEM HS:1024BX3 32
- 4.4 Characterizing Camera Performance 33
  - 4.4.1 Thermal Counts and Clock-Induced Charges 35
  - 4.4.2 Readout Noise 37
  - 4.4.3 Real Gain 37
  - 4.4.4 Stray Light 38

5 Identifying Single Atoms 41
- 5.1 Local Maxima Created by a Low-Pass Filter 42
- 5.2 Size of Clusters 44
- 5.3 Orientation of Clusters 45
- 5.4 Sum over Pixel Values of Clusters 45
- 5.5 Comparison to Experimental Data 46

5.6 Possible Reasons for Indistinct Experimental Results 48
5.7 Planned Improvements 49

6 Conclusion & Outlook **51**

A Technical Specifcations **53**
A.1 ProEM HS:1024BX3 53
A.1.1 Excerpts from Data Sheet 53
A.1.2 Specification Sheet 56
A.1.3 Influence of Vertical Shift Speed on CICs 57

Bibliography **59**

List of Figures

2.1 Level Structure of ^{39}K. 14
2.2 Scattering Potentials Involved in a Feshbach Resonance. 15
2.3 Imaging Transitions and Breit-Rabi Diagram of ^{39}K. 16
2.4 Simulated Examples of Atomic Random Walk. 19
2.5 Atom Diffusion During Random Walk. 20
2.6 Influence of the PSF. 21

3.1 Readout Process of a CCD Sensor Chip. 24
3.2 Noise Sources of (EM) CCD Cameras. 25
3.3 Probability Distributions for the EM Gain Register Output. 27
3.4 Examples of Binarized Single Atom Signals. 28
3.5 Statistical Overview over Simulated Single Atom Signals. 29

4.1 Confinement of the 2D BEC. 31
4.2 Imaging Setup for the DMD, Absorption and Fluorescence Imaging. 33
4.3 Internal Structure of a Frame Transfer EM CCD Camera. 34
4.4 Dark Noise Pattern of the Camera's CCD Chip. 35
4.5 Estimation of the Camera's Dark Current and CICs. 36
4.6 Dark Noise Pattern of the Camera's CCD Chip with Cleaning. 37
4.7 Noise from Stray Light Sources. 38

5.1 Binarized Simulated Atom Signals in Real Noise Data. 41
5.2 Working Principle of the Low-Pass Filter Method. 42
5.3 Statistics and Performance of the Low-Pass Filter Method. 43
5.4 Statistics and Performance of the Cluster Method. 44
5.5 Statistics of the Cluster's Orientation. 45
5.6 Fluorescence Images of Depleted Densities. 46
5.7 Analysis of Experimental Data based on Cluster Sizes and Pixel Values. 47
5.8 Analysis of Experimental Data Based on Poisson Statistics. 48

A.1 Data Sheet, Page 1. 53
A.2 Data Sheet, Page 3. 54
A.3 Quantum Efficiency. 55
A.4 Certificate of Performance for our Camera. 56
A.5 Influence of the VSS on the Creation of CICs. 57

1 Introduction

While well-known, simple laws describe the dynamics and interaction of particles, the mathematical description quickly becomes intractable if many particles interact with each other. In thermal equilibrium the problem can be tackled by reducing the description of the system to suitable macroscopic equilibrium state variables, like pressure or temperature, and describing the system's evolution in terms of these ensemble observables instead of the dynamics of individual particles. However, because these state variables are well-defined only in thermal equilibrium, this approach is valid only if the system's dynamics is slow compared to the thermal redistribution processes, so that the system can always be described as in thermal equilibrium.

However, many interesting physical phenomena cannot be explained by these simplified models, but require a full non-equilibrium description. This is the case for the formation of structures in the early universe [1, 2], dynamics close to a non-thermal fixed point [3, 4], and the process of thermalization itself [5, 6]. Such phenomena have to be described by suitable non-equilibrium state functions to capture features like transport processes. However, systems that exhibit these behaviours are experimentally hard (or even impossible) to replicate, making it difficult to directly test theoretical predictions.

Recently, experimental platforms became available that allow to implement systems that model aspects of non-equilibrium phenomena. One route to experimentally investigate processes important to the very early stages of the universe is to replicate the enormous energies and densities of that era in heavy-ion collisions, a research field of high-energy physics. The other platform is on the other end of the energy scale, namely ultracold quantum gases. Ultracold quantum systems can be controlled and tuned particularly well, making them very versatile and successful model systems [7, 8]. Many processes can already be understood in reduced dimensions. While 1D experiments already offer access to various phenomena [9, 10], 2D experiments allow for more complex dynamics [11, 12] while still allowing efficient detection. One particularly interesting atomic species is ^{39}K, as the interactions of the atoms can be adjusted using a broad magnetic Feshbach resonance [13], which allows to finely tune the s-wave scattering length of the atoms by applying an external magnetic field.

In our group, a two-dimensional ^{39}K Bose-Einstein condensate is used to investigate non-equilibrium effects induced by parametric resonance. In these experiments, harmonic driving of the condensate excites the primary resonant momentum mode, which in turn can populate secondary and tertiary modes. Ultimately this is predicted to result in a cascade to high momenta [14], in which few particles with high momenta carry away the energy. To study the growth rates of primary, secondary and tertiary excitation as well as the energy cascades, we need to access the condensates momentum distribution and be able to detect very low densities, down to the single-particle level.

In our experiment, the condensate's momentum distribution can be accessed by the technique of phase-space imaging [15]. A time-of-flight measurement in a weakly confining harmonic trap yields the momentum distribution after a quarter of the trap's period. This places particles with high momenta at the edges of the trap. The few high-momentum particles we are looking for will therefore also be distributed over a large area. These low densities are not accessible with absorption imaging, which up to now was the only imaging technique of the experiment.

This thesis establishes fluorescence imaging in our experiment with the aim of reaching single-atom resolution, and thus gain access to densities below the detection limit of absorption imaging. In our experiment this task is complicated further because, in contrast to other experiments, the atoms are not confined in an optical lattice [16, 17] or in optical tweezers [18] during imaging but propagate freely.

This thesis is structured as follows: We will start by calculating the average fluorescence signal of a single atom of ^{39}K in terms of photons and photoelectrons in chapter 2. To detect the few photons scattered by a single atom an Electron Multiplying CCD camera is employed, the technical details and noise sources of which will be discussed in general in chapter 3, and for our specific imaging setup and camera in chapter 4. Then we will benchmark different methods to identify single atoms on simulated single-atom signals, and compare the findings with experimental data in chapter 5. Finally we discuss possible reasons for the differences between simulation and experiment and give an outlook on the next steps.

2 Fluorescence Imaging of ^{39}K

This chapter gives an overview of the properties of ^{39}K. Then the average fluorescence signal of single ^{39}K atoms is calculated in terms of photoelectrons created on the camera's CCD chip, considering the atom's scattering rate and dipole radiation pattern as well as technical effects like the imaging setup's numerical aperture and the camera's quantum efficiency. Lastly, to estimate the spread of the signal, the atom's diffusion during imaging and the effect of the imaging system's point spread function are modelled and single atom fluorescence signals simulated.

2.1 Properties of ^{39}K

Potassium is an alkali metal with atomic number $Z = 19$. Its three naturally occurring isotopes are ^{39}K, ^{40}K and ^{41}K, of which ^{39}K and ^{41}K are bosonic. The BECK experiment (**B**ose-**E**instein **C**ondensate ^{39}**K** experiment) for which this thesis is conducted is based on a ^{39}K Bose-Einstein Condensate. This atomic species is interesting because of its broad magnetic Feshbach resonance, which allows to tune the atom's scattering length. Depending on the experimental scenarios the scattering length is tuned by adjusting an external magnetic field. This field however also influences the internal energy levels of the atoms. To achieve effective signal collection independent of the applied field, the imaging transitions have to be chosen carefully.

2.1.1 Level Structure

Potassium is listed in group 1 of the periodic table and thus has only one valence electron. Its ground state electron configuration is given by $1s^2 2s^2 2p^6 3s^2 3p^6 4s^1$ or $[\mathrm{Ar}]4s^1$. Since the inner shells are all completely occupied they neither contribute to the total electron spin S, nor to the total orbital angular momentum L. Thus the quantum number of the total electronic angular momentum J, corresponding to the operator $\hat{J} = \hat{L} + \hat{S}$, can only take the value $1/2$ where $L = 0$ and $S = 1/2$. A detail of the level structure of ^{39}K can be seen in fig. 2.1. The electronic ground state is noted by $^2S_{1/2}$. The two first excited states, where the valence electron is excited to the next higher orbital ($L = 1$), are given by $^2P_{1/2}$ and $^2P_{3/2}$. The transitions from the ground state to these excited states are called the D_1 line with $\lambda_{\mathrm{D1}} = 770.108\,\mathrm{nm}$, and the D_2 line with $\lambda_{\mathrm{D2}} = 666.701\,\mathrm{nm}$.
We also have to consider the hyperfine splitting. The nuclear spin of ^{39}K is $I = 3/2$. The operator for the total angular momentum is given by $\hat{F} = \hat{J} + \hat{I}$, and its quantum number can take the values $|J - I| \leq F \leq |J + I|$. Thus the hyperfine structure splits states with $J = 1/2$ into two states where $F = 1, 2$, and states with $J = 3/2$ into four states where $F = 0, 1, 2, 3$ (see again fig. 2.1). Each of these states again is split into substates, corresponding to the $2F+1$ possible orientations of the total angular momentum described by the quantum number m_F. Without an external magnetic field, these $2F + 1$ substates are degenerate. However, if a magnetic field is applied, these substates experience an energy shift depending on their m_F, which is called the Zeemann effect. At our experiment the created condensate consists of atoms in the state corresponding to $\left|F, m_F\right\rangle = \left|1, -1\right\rangle$ at low magnetic fields.

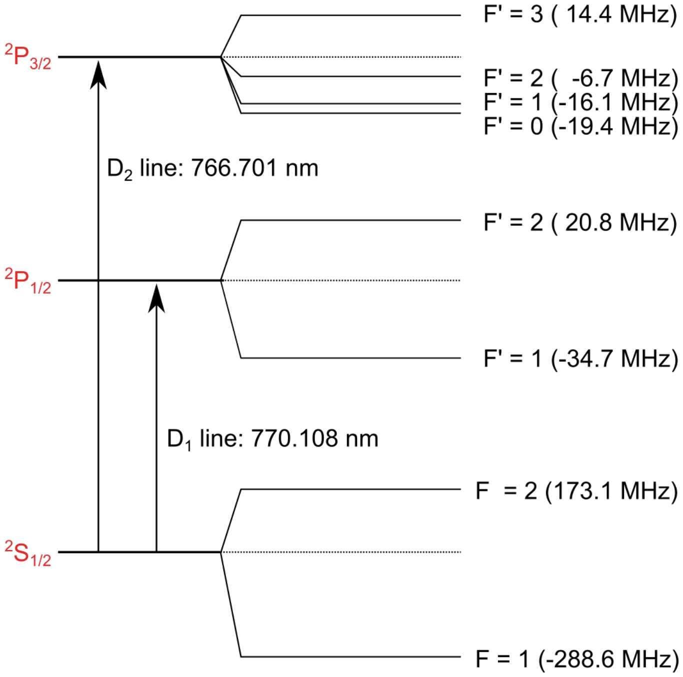

FIGURE 2.1. **Level Structure of ^{39}K.** The transitions from the electronic ground state $^2S_{1/2}$ to the first two excited states $^2P_{1/2}$ and $^2P_{3/2}$ are called the D$_1$ and D21 lines. The hyperfine structure splits the levels further into substates depending on the total magnetic moment F. These hyperfine states each consist of $2F+1$ substates, each associated with a quantum number m_F. These substates are degenerate for no external magnetic field. An external magnetic field lifts this degeneracy via the Zeemann effect.

2.1.2 Feshbach Resonances

Another feature of ^{39}K is that its s-wave scattering length a can be influenced by a property called a (magnetic) Feshbach resonance. It allows to tune the scattering length of the atoms by adjusting an external magnetic field.

Scattering of two atoms is described using a scattering potential. If a bound (molecular) state exists with an energy close to the combined energy of the two incoming atoms (see fig. 2.2, left), an unstable compound state can be formed with very short life time. This is the so-called Feshbach resonance. The atoms consequently experience the scattering potential longer than they would have without the unstable bound state, meaning that the influence of the scattering process on their wave functions is greater. This alters the scattering length associated with the process. In a magnetic Feshbach resonance the resonance condition can be externally tuned via the Zeemann effect. For a more in-depth discussion see [19].

In ultracold atomic many-body systems only s-wave scattering processes can occur due to the extremely low kinetic energies of the atoms. For scattering processes between atoms in the same m_F substate, the dependence of the s-wave scattering length a on the magnetic field B around a Feshbach resonance centered at B_0 is described by [20]

$$a(B) = a_{\mathrm{bg}} \left(1 - \frac{\Delta}{B - B_0}\right) \ , \tag{2.1}$$

where a_{bg} is the background scattering length and Δ the width of the resonance. Feshbach resonances for ^{39}K are shown in (fig. 2.2, right), with values for a_{bg}, Δ and B_0 taken from

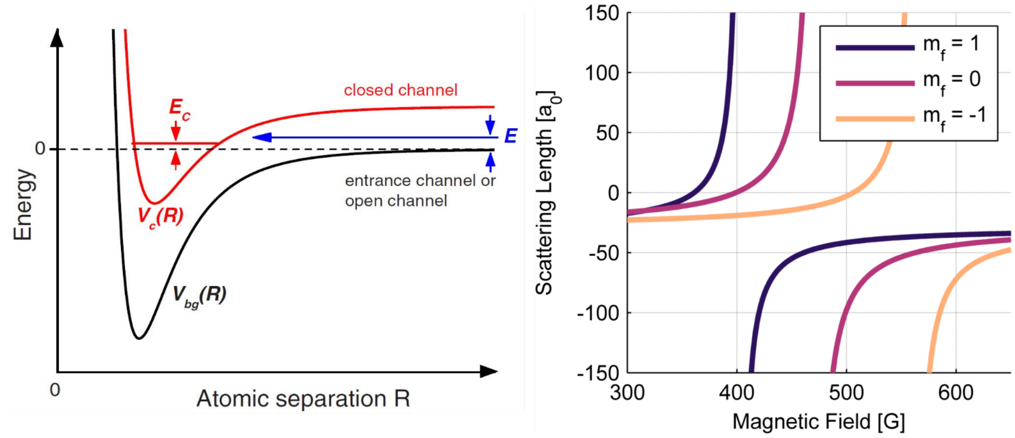

Figure 2.2. **Scattering Potentials Involved in a Feshbach Resonance. Left:** If a molecular state exists that is energetically close to the energy of the two scattering atoms, an unstable bound state can form. The formation of that state influences the effect of the scattering process on the atomic wave functions, which alters the scattering length associated with the process. Figure taken from [19]. **Right:** Broad Feshbach resonances for ^{39}K substates between 300 G and 650 G. In the experiment the atoms are in the substate defined at zero field as $|F, m_F\rangle = |1, -1\rangle$, and so the Feshbach resonance centered at 550 G can be used to tune the scattering length.

[21]. On the BECK experiment the broad resonance around 550 G ($m_F = -1$) is used, which allows to tune a both to positive and negative values.

2.1.3 Imaging Transitions

Imaging transitions ideally are chosen such that a closed optical cycle is established, where excited atoms only fall back to their initial state. This ensures that atoms do not leave the imaging cycle and the signal continuously increases over time. If the optical cycle is not closed however atoms decay into states that can not be addressed by the imaging light, and the signal decays. Closed optical cycles are not easily implemented for arbitrary states and arbitrary external fields. To image the ^{39}K BEC at the moderate magnetic fields around our Feshbach resonance we use an approximately closed four-level optical cycle. A sketch of the imaging scheme can be seen on the left of fig. 2.3.
In fig. 2.3 on the right a Breit-Rabi diagram shows the energy splitting of the $^2S_{1/2}$ ground state and $^2P_{3/2}$ excited state hyperfine manifolds due to the Zeeman effect. Depending on their m_F quantum number, the energies of the substates are shifted by an external magnetic field. The two transitions marked by arrows are driven by σ^+- and σ^--polarized light. The BEC's atoms are initially in the state

$$|g_-\rangle = |m_I, m_J\rangle = \sqrt{p}\,|-1/2, -1/2\rangle + \sqrt{1-p}\,|1/2, 3/2\rangle \approx |-1/2, -1/2\rangle \ , \tag{2.2}$$

where $p \in [0\,1]$ depends on the magnetic field ($p \approx 0.98$ at 550G.). The main imaging light drives the transition to the state $|e_-\rangle = |-3/2, -1/2\rangle$ with σ^--light. From this state however the atoms can also decay into the the dark state

$$|g_+\rangle = \sqrt{p}\,|1/2, -3/2\rangle + \sqrt{1-p}\,|-1/2, -1/2\rangle \approx |1/2, -3/2\rangle \tag{2.3}$$

since this state also has a (small) $|-1/2, -1/2\rangle$ contribution. To stop the atom population from draining into this dark state a repumper transition is driven with σ^+ polarized light to transfer atoms into the second excited state $|e+\rangle = |3/2, -3/2\rangle$, from which they can decay

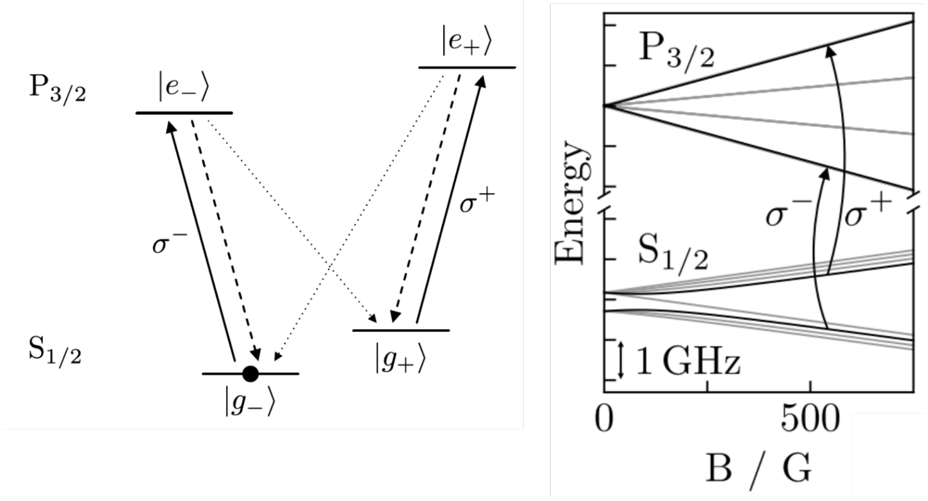

FIGURE 2.3. **Imaging Transitions and Breit-Rabi Diagram of ^{39}K. Right:** Four-level scheme employed to realize an almost closed optical cycle for imaging.**Left:** Energy splitting of the hyperfine manifolds of the $^2S_{1/2}$ and $^2P_{3/2}$ states of ^{39}K caused by the Zeeman shift. Figures adapted from [22].

back intro the $|g_-\rangle$ state. This closes the optical imaging cycle in good approximation. For a more detailed discussion see [22].

2.2 Estimating the Mean Signal per Single Atom

To get a first idea about the signal we can expect per atom we need to estimate the amount of photons our imaging setup will collect per atom, and how many photoelectrons those will create. However, the interaction of atoms and light is a stochastic process and it is not possible to exactly predict how many photons a particular atom will scatter. Therefore we can only calculate the mean signal per atom, starting with the scattering rate.

2.2.1 Scattering Rate

The photon scattering rate γ of a two-level system coupling to a oscillating electric field is given [23] by

$$\gamma = \frac{\Gamma}{2} \cdot \frac{I/I_{\text{sat}}}{1 + I/I_{\text{sat}} + (\frac{2\delta}{\Gamma})^2}, \tag{2.4}$$

where Γ is the natural linewidth of the transition, I is the imaging intensity, I_{sat} is the saturation intensity, and δ is the detuning from resonance. When imaging with intensities well over I_{sat} and very close to resonance, eq. 2.4 reduces to $\gamma \approx \frac{\Gamma}{2}$. The natural linewidth of the primary imaging transition is $\Gamma = 2\pi \cdot 6\,\text{MHz}$ [21], which gives us a scattering rate of

$$\gamma = \frac{2\pi \cdot 6\,\text{MHz}}{2} \approx 18.8\,\text{MHz} \equiv 18.8\,\frac{1}{\mu\text{s}}. \tag{2.5}$$

Thus, if our imaging intensity is high enough, we ideally can expect for an imaging pulse of $10\,\mu$s 188 scattered photons per atom on average.

2.2.2 Numerical Aperture and Dipole Radiation Pattern

Of the scattered photons only those can contribute to the signal that are collected by the imaging system. The numerical aperture (NA) of an imaging system is a measure for the greatest angle under which the system can still emit or collect light. The NA of an optical system with opening angle α working in a medium with refractive index n is defined as

$$\mathrm{NA} = n \cdot \sin(\alpha). \tag{2.6}$$

The NA of our imaging setup is limited by the objective that has a numerical aperture of 0.5, which corresponds to an opening angle of $2\alpha = 2 \cdot 30°$. For a uniform photon emission in every direction 6,7 % of the photons would be collected by our objective. However, the atom's emission is not uniform. Due to the magnetic field, which is parallel to the imaging path, the atomic dipoles are not randomly oriented but aligned with the field. This changes the dipole radiation pattern of the atoms. For circularly polarized light the emission along the magnetic field is enhanced, and thus the fraction of photons entering the objective is increased. The dipole radiation pattern for circularly polarized light follows [24]

$$\hat{I}(\theta) = \frac{I(\theta)}{I_0} = \frac{3}{8}\frac{1+\cos^2(\theta)}{2\pi}. \tag{2.7}$$

The total signal we can collect is calculated by integrating over the solid angle covered by the objective, taking into account the angular dependence of the emission pattern:

$$\begin{aligned} S &= \int_0^{2\pi}\int_0^{\alpha} \hat{I}(\theta)\sin\theta \,\mathrm{d}\theta\,\mathrm{d}\phi \\ &= \int_0^{2\pi}\int_0^{\alpha} \frac{3}{8}\frac{1+\cos^2(\theta)}{2\pi}\sin\theta\,\mathrm{d}\theta\,\mathrm{d}\phi \\ &= \frac{3}{8}\int_0^{\alpha} 1+\cos^2(\theta)\sin\theta\,\mathrm{d}\theta \\ &= -\frac{3}{8}\int_1^{\cos(\alpha)} 1+u^2\,\mathrm{d}u \\ &= \frac{3}{8}\left(\frac{4}{3} - \cos(\alpha) - \frac{1}{3}\cos^3(\alpha)\right) \end{aligned} \tag{2.8}$$

With $\alpha = 30°$, our objective collects 9.4 % of the radiated photons.

2.2.3 Transmission Through Optical Components

Between the fluorescing atoms and the camera are several optical components. Their limited transmission T and reflectance R at the imaging wavelength 767 nm further decrease the number of photons reaching the camera. The components are:

- Experimental Chamber (glass)
- Objective, $T \approx 91\,\%$
- Mirror, $R \approx 99.7\,\%$
- Lense, $T \approx 99.7\,\%^2 \approx 99.4\,\%$
- Dichroic Longpass Mirror, $T \approx 97.8\,\%$
- Dichroic Shortpass Mirror, $T \approx 98.1\,\%$

- Shortpass Filter, $T \approx 98.7\,\%$
- Single Notch Filter, $T \approx 97.6\,\%$

These components are further discussed in section 4.2. Overall, we estimate that $T_{\text{total}} \approx 82\,\%$ of the photons emitted in the correct direction reach the camera.

2.2.4 Quantum Efficiency

The quantum efficiency (QE) of a CCD sensor defines the ratio of incoming photons and created photoelectrons. It depends on CCD chip temperature and imaging wavelength. A QE of 1 (or 100 %) describes the ideal case in which every photon reaching the CCD array creates one photoelectron. In practice, the quantum efficiency is below one. To estimate the single atom signal, a QE of 0.8 is used. The quantum efficiency of the camera used in the experiment as measured by the manufacturer can be found in appendix A.1.1.

2.2.5 Expected Photoelectrons per Atom

Combining the above discussed considerations, with our setup ideally

$$0.094 \cdot 0.82 \cdot 0.8 \cdot 18.8\,\text{MHz} \cdot \Delta t \approx 1.16\,\text{photoelectrons}\,/\mu\text{s} \equiv 12\,\text{photoelectrons}\,/10\,\mu\text{s} \tag{2.9}$$

can be expected on average per single atom. However, these photoelectrons will not be generated on a single pixel but will be spread over several due to two main effects, which will be discussed next.

2.3 Estimating the Signal Spread

To estimate the spread of the signal from a single atom, two main contributions have to be taken into account. First, the atoms are not fixed during the imaging process but can move freely in a very shallow trapping potential of approximately 5.5 Hz. While scattering photons the atoms perform a random walk that leads to a diffusive motion, spreading the photons over several pixel. Furthermore the point spread function of the imaging has to be taken into account, which also influences the signal distribution.

2.3.1 Influence of Initial Thermal Velocity

The estimated initial temperature of the 2D BEC is on the order of 70 μK. Assuming that the BEC can be approximately described as an ideal gas, the velocity spread of the atoms follows a Maxwell-Boltzmann distribution. A temperature of 70 μK corresponds to a mean velocity of $v_{\text{mean}} \approx 0.0062\,\text{m/s}$. Therefore the initial velocities of the atoms is very likely well below the recoil velocity of a single photon recoil of $\Delta v_{\text{recoil}} \approx 0.0133\,\text{m/s}$, which is why in the following simulation of the atoms' random walk the initial velocity will be neglected and set to zero. This of course does not apply to atomic gases at higher temperatures.

2.3.2 Influence of Doppler Shifts

From absorbing one photon an atom's velocity changes by

$$\Delta v = \frac{\text{h}}{\lambda m} \approx 0.0133\,\text{m/s}\ . \tag{2.10}$$

The natural linewidth of the imaging transition is 6 MHz. The Doppler effect shifts the atoms one linewidth away from the resonance for atoms with a velocity of $v_{\text{rel}} = 4.6\,\text{m/s}$ relative to the imaging photons. Since $v_{\mathrm{rel}} \approx 345\Delta v_{\mathrm{recoil}}$, an atom at rest would have to receive 345 photon kicks towards an imaging beam for this to happen. However, since the atoms are illuminated from two opposing directions, this scenario is unlikely and the influence of Doppler shifts on the scattering rate is neglected in the following estimations. For atoms with non-negligible initial velocities however this naturally does not apply. This again underlines the importance to make sure that the cloud to be imaged is ultracold.

2.3.3 Influence of Diffusive Motion

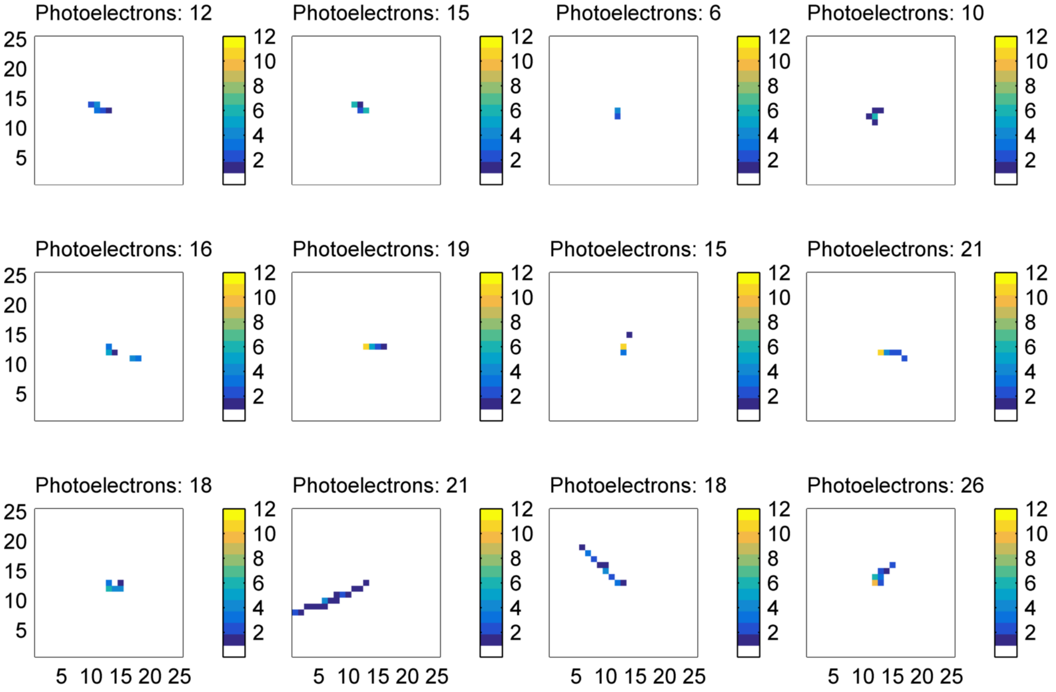

FIGURE 2.4. **Simulated Examples of Atomic Random Walk.** Simulated single atom fluorescence signals for different imaging durations (upper row 10 μs, middle row 15 μs, lower row 20 μs). On average, 12 photoelectrons are created in 10 μs. Scattering light from the imaging beams (comming from left and right) creates a diffusive motion. Each emitted photon has to pass the imaging system and then has to create a photoelectron on the camera in order to be detectable. The probabilities for these conditions are given by the transmittance of the setup, the NA and the QE. Above each frame the total number of created photoelectrons is given. Lastly the atomic signal is mapped on a grid, analogous to the camera pixels. One pixel corresponds to $(0.46\,\mu\mathrm{m})^2$ in the atom plane. Effects of the imaging setup's point spread function are not included in these example simulations.

The scattering of photons during imaging induces on the atoms a random walk in velocity space. This motion will smear the photon signal created by an atom over several pixels. To estimate this the random walk is modelled, assuming no initial atom velocity as justified above.

During imaging, one atom absorbs and re-emits on average 18 photons/1 μs (see section 2.2.1) with a recoil velocity of $\Delta v_{\mathrm{recoil}} \approx 0.0133\,\mathrm{m/s}$ from the imaging light. The BEC is illuminated from two opposing directions using an retro-reflected beam along the y-axis (see section 4.2), such that the atoms will absorb photons from both directions. The emitted photons are radiated according to the dipole radiation pattern discussed in section 2.2.2. Emission along the z-axis is more probable than emission in the xy-plane. To confine the atoms in z-direction during imaging, the pancake trap is turned on slightly. Therefore diffusion along this direction is suppressed and not considered here.

In the xy-plane the emission probability is radially symmetric. The BEC is imaged along the z-axis of the system, meaning that the signal is projected onto the xy-plane. If the imaging beams from the two directions have equal intensities, all scattering forces acting in the xy-plane are balanced and the expectation value of the velocity $\langle v \rangle$ is zero. The variance $\langle \Delta v \rangle^2 = \left\langle v^2 \right\rangle$ however is not, so that the atoms will undergo a diffusive motion.

A model of the random walk was implemented in MATLAB. The time between scattering events in the model is fixed and corresponds to the scattering rate γ in eq. 2.5. For each scattering event values for photon absorption/emission angles ϕ (in the xy-plane) and θ (angle between direction of emission and z-axis) are drawn and the atom velocity calculated. Kicks from photon absorption are always along the x-axis ($\theta = \pi/2$, $\phi = 0$ or π), kicks from emissions are drawn according to the dipole radiation pattern. Then, the atom is propagated in the xy-plane until the next scattering event changes the velocity again. For each emitted photon random numbers are drawn to decide whether the photon passes the objective and reaches the camera (probability of $0.094 \cdot 0.82 = 7.5\,\%$ from transmission and QE) and whether it creates a photoelectron on the CCD array (probability of $80\,\%$). Lastly, the photon positions are binned into "pixels" the size of $(0.46\,\mu\mathrm{m})^2$, corresponding to the pixel size in the atom plane of the camera (see section 4.2). Examples of single atom signals computed in this way can be seen in fig. 2.4.

To quantify the signal spread caused by the diffusion 10000 simulated runs runs were performed, the final positions plotted for different diffusion times and fitted with a Gaussian curve. This can be seen in fig. 2.5. The diffusion along the imaging beams produces a wider probability distribution than the diffusion perpendicular to it. Even for perfectly balanced beams, the probability distribution along the beams after an imaging duration of $10\,\mu$s has already a width of $1.4\,\mu$m (ca. 3 pixels) along the imaging beam axis. When choosing an imaging duration we thus have to find a compromise between the average signal per atom and the signal spread.

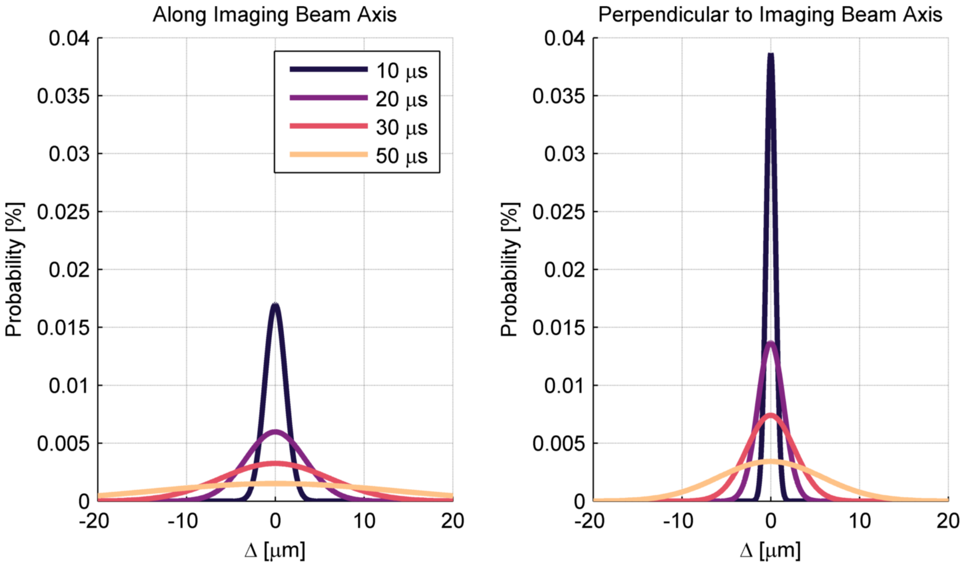

FIGURE 2.5. **Atom Diffusion During Random Walk.** From 10.000 simulated runs the positions were extracted to get an estimation for the atomic diffusion, and thus the signal spread, for imaging durations of 10, 20, 30, 50 μs.

2.3.4 Influence of Point Spread Function

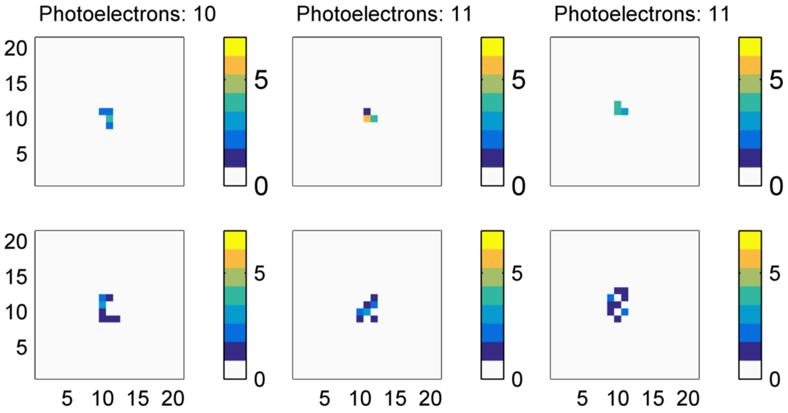

Figure 2.6. **Influence of the PSF. Top:** Examples of photoelectron distribution from single atoms for an imaging duration of 10 μs. **Bottom:** Photoelectrons redistributed by the PSF of the imaging system.

Not only the diffusive motion of the atoms influence the signal spread, but also the point spread function (PSF) of the imaging system. In a perfect imaging system, a point source will be also imaged as a point. In real systems however the image of a point source will be spread broader due to for example aberrations and the NA of the imaging system. The width and shape of the PSF depends on the optical components used and is highly sensitive to their alignment. Thus, the PSF will further distribute the fluorescence signal from the atom: Even if an atom has not moved "off" a pixel, the scattered photons can be distributed over pixels near by.

The PSF of the imaging system used has a width of approximately 4 pixels. This also has to be included in the simulation. First the atom's random walk is simulated, then every created photoelectron is redistributed to other pixels according to probabilities given by the PSF. The PSF redistributes the photons independently of their diffusion direction, thus it happens more often that the signal is spread over pixels that are not next neighbours to each other but separated by empty pixels. Examples of the PSF influence can be seen in fig. 2.6.

This simulation only covers the signal collected from atoms - the noise was not considered. However, to find the ideal imaging parameters, the noise also has to be taken into account. Apart from stray light there are several technical noise sources specific for EM CCD cameras, which have to be understood in order to minimize them.

3 Detecting Low Photon Signals

The few photons collected of an individual atom are focused onto a camera's CCD chip, where they produce just a handful of photoelectrons. On a conventional CCD camera, these faint signals would be lost in the noise of the readout electronics. Therefore we have to use an Electron Multiplying CCD camera which amplifies the photoelectrons before reading them out. In this chapter, the working principle and the noise sources of (EM) CCD cameras are described. Then the electron multiplication process is outlined and its effects and implications discussed.

3.1 Charge Coupled Device Sensors

A Charge Coupled Device (CCD) Sensor detects photons by converting them into electrons via the photoelectric effect (so-called photoelectrons), storing the electrons on pixels and then converting the pixel charge into a digital pixel value.

For the basic structure and working principle of a CCD sensor see fig. 3.1. CCD sensors consist of photoactive silicone, topped with an insulating layer and an array of electrodes, each electrode constituting one pixel. During the image acquisition a positive voltage is applied to the electrodes. Incoming photons create free electrons in the photoactive layer which are stored in the potential wells below the electrodes. The ratio between photons and created photoelectrons is called quantum efficiency and lies below one.

In contrast to CMOS-sensors where each pixel has its own readout electronics, CCD sensors only have one Analog-to-Digital Converter (ADC). To read out an image, each pixel's charges have to be conveyed to the readout. This is done by applying positive so-called clock voltages to neighbouring pixels one row closer to the readout, thus shifting the electrons vertically row by row onto a readout register. Once on this register, the electrons are shifted horizontally towards the readout. The shifting process introduces noise into the image. Since pixels further away from the readout electronics have to be shifted more often, the created noise is not distributed evenly over the image. This effect is discussed further in section 3.2.2. Finally the ADC converts the photoelectrons into a digital signal for one pixel at a time.

During this process of taking an image and reading it out, noise from multiple sources accumulates. The main contributions will be discussed next.

3.2 Noise Sources of CCD Cameras

Since we will be searching for signals on the order of just a few photoelectrons per pixel, it is essential to understand and minimize the noise sources. Noise can be introduced at different stages while taking a picture. To reduce the amount of stray photons the camera should be shielded using beam blocks, cladding or, if the stray light has another wavelength than the signal photons, optical filters. Other noise sources are thermally created electrons, charges created during the readout process, and the noise of the readout electronics. These effects are of technical origin and depend on the camera. They can be reduced by choosing the optimal camera settings. An overview over the noise sources of CCD sensors is sketched in the upper part of fig. 3.2.

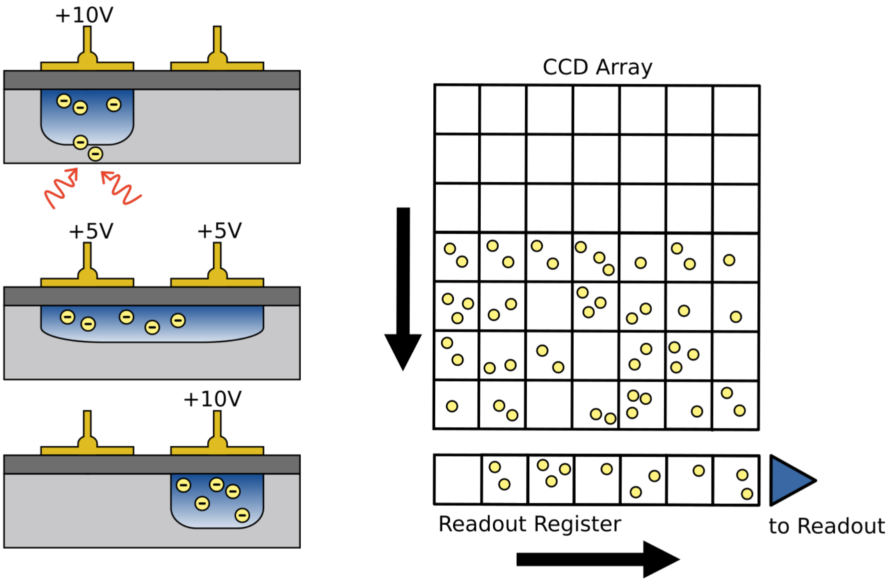

FIGURE 3.1. **Readout Process of a CCD Sensor Chip.** Free electrons are created by incident photons. During imaging a positive voltage is applied to the pixels and the photoelectrons are collected in the thus created potential wells (left). To read out the pixel charge the electrons are transported to the readout electronics. This is done by vertically shifting a row from the CCD array onto a readout register by applying positive voltages to neighbouring pixels. Then the pixels are shifted horizontally towards the readout node (right). The process is repeated until all pixels are read out. Consequently, pixels at the top of the array have to be shifted more often, resulting in a distinct noise distribution over the image.

3.2.1 Thermal Counts

Thermal counts (also called dark counts) are counts that are not generated by photons but by thermal energy. Free electrons are created in the photoactive semiconductor region of the CCD array and are stored in the pixels potential wells. They can not be distinguished from photon-generated electrons and contribute to the pixel value. The number of thermal electrons created is temperature dependent; to minimize noise from dark counts CCD cameras are typically cooled to temperatures of $-50\,^\circ$C and below. Dark counts are created continuously, not only during the period where the camera shutter is opened during imaging. Thus, a quick readout of the image as soon as it is taken is essential. However, a faster readout also means excess noise from clock-induced charges and readout noise.

3.2.2 Clock-Induced Charges

During the image readout, the electrons on each pixel are shifted or "clocked" towards the readout electronics. For each shifting step, voltages have to be applied to the pixels. These voltages can, with a very low probability, create further electrons even on pixels that were empty otherwise. These electrons are called Clock-Induced Charges (CICs). They will be read out like regular photoelectrons and can not be identified on individual pixels. However, since pixels further away from the readout have to be shifted more often, one can find a distinctive noise pattern over the CCD array. The creation of CICs is minimized by choosing the optimal period, amplitude and shape of the clock voltage by the manufacturer of the camera and can afterwards only be influenced by adjusting the vertical shift speed (VSS) and

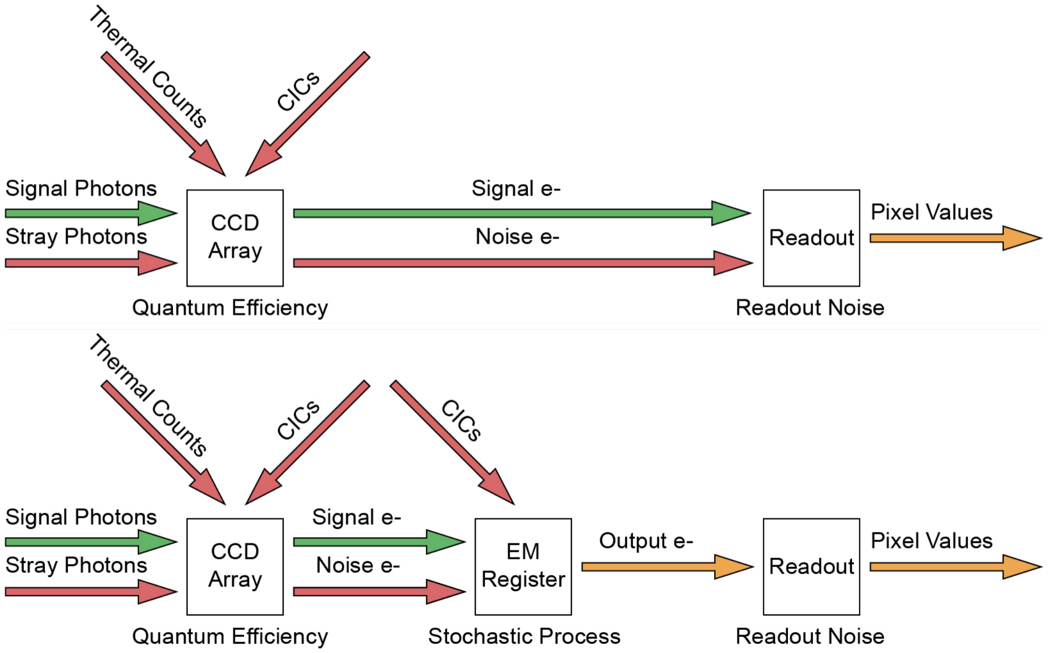
Thermal Counts
CICs
Signal Photons
Stray Photons
CCD Array
Quantum Efficiency
Signal e-
Noise e-
Readout
Readout Noise
Pixel Values
Thermal Counts
CICs
CICs
Signal Photons
Stray Photons
CCD Array
Quantum Efficiency
Signal e-
Noise e-
EM Register
Stochastic Process
Output e-
Readout
Readout Noise
Pixel Values

FIGURE 3.2. **Noise Sources of (EM) CCD Cameras.** CCD cameras (**top**) and EM CCD cameras (**bottom**) are affected similarly by noise. Noise counts from stray photons have to be reduced by shielding the camera from unwanted light sources. The influences of thermal counts, CICs and readout noise depend on the camera used and can be reduced (within the technical possibilities) by optimizing camera parameters. EM CCD cameras can be used to amplify small signals above the readout noise. However, noise electrons will be amplified as well. Additionally, the creation of CICs is also possible in the EM gain register. The electron multiplication is a stochastic process, which makes it impossible to infer the number of input electrons from the amount of output electrons.

the readout rate. The faster the pixels are moved over the CCD array, the higher the number of created CICs. If the frame rate is not important it is therefore often favorable to use the slowest possible readout speed, tolerating the accumulation of more dark counts.

3.2.3 Readout Noise

While Dark Counts and CICs cause additional counts, the noise introduced by the readout electronics adds an uncertainty to the final pixel values. It only depends on the readout rate and is typically on the order of 5 to 30 electrons. This makes the direct detection of very low-photon signals like the fluorescence of a single atom impossible, as the few created photoelectrons will be lost in the readout noise. To circumvent this one can use an electron multiplying CCD camera that amplifies the photoelectrons before readout, which are described in the following section.

3.3 Electron Multiplying CCD Cameras

Very faint signals on the order of just a few photons are not detectable with regular CCD sensors as the few photoelectrons would be hidden in the noise of the readout electronics. To overcome this limitation, electron multiplying CCD (EM CCD) Cameras first multiply electrons out of the readout noise floor before converting them into pixel values. Certain noise electrons, however, are amplified as well.

Image acquisition on EM CCD cameras works like acquisition for regular CCD cameras. Once a row of electrons is shifted onto the readout register, however, the electrons are not read out immediately, but are first accelerated through an electron multiplication register. There the original input electrons create more electrons by an avalanche effect. Thermal counts and CICs, both created on the CCD array, are amplified in the EM gain register just like photoelectrons. The benefit the EM mode offers is that faint signals are not immediately lost in the readout noise. Additionally, the creation of CICs is also possible in the EM gain register. Since the charges are created somewhere in the register, they will effectively have a lower gain than charges that were created already on the CCD chip. The CICs created in the gain register will not contribute to the noise gradient over the picture from the CICs created by the shifting process on the array, but will affect all pixels equally. An overview over noise sources of EM CCD cameras is sketched in the lower part of fig. 3.2.

The electron multiplication is a stochastic process - it is not possible to predict the exact amount of output electrons from the input electron number. The probability distribution for output electrons created by a given number of input electrons depends on the acceleration voltage applied, making it possible to tune the mean multiplication factor, the so-called electron gain. The probability distribution follows ([25], [26])

$$P_n(x) = \frac{x^{n-1}\,\mathrm{e}^{-x/g}}{g^n(n-1)!}, \tag{3.1}$$

where n is the amount of input photoelectrons, x the number of output electrons, and g the electron gain. The expectation value of this distribution is ng, the variance ng^2. In fig. 3.3 on the left the probability distributions describing the EM gain register output are shown for $n = 1, 2, 3, 4$ input electrons. The distributions for different numbers of input electrons overlap considerably. This makes it impossible to precisely determine the initial number of electrons on a pixel. Especially in the few-photon regime it thus makes sense to only distinguish between pixels that were empty and pixels that held photons. This idea will be further explained in the next section.

3.4 Image Binarization

After the electron multiplication it is not possible to infer the number of initial input electrons from the EM registers output. Especially in the regime of a few photoelectrons per pixel the only reasonable distinction is between "probably empty" pixels, and pixels that "probably held electrons". However, because of the readout noise, it is not trivial to decide which pixels were empty. To differentiate between empty and not empty we have to chose an appropriate cutoff in pixel value, above which a pixel has a significant change of having had at least one electron. Pixels with a value above the cutoff will be set to one, is the value below the cutoff the pixel will be set to zero. This process will be called "binarization".

A histogram of a typical EM dark image ($g = 310$, taken with the camera shutter closed) can be seen on the right of fig. 3.3. The Gaussian peak on the left of the histogram corresponds to the empty pixels of the image. The peak is not centered at zero because the camera applies an offset. The width of the peak depends on the camera's readout noise. A bigger readout noise broadens the peak because it allows more different pixel values for empty pixels.The tail to the right of the Gaussian peak corresponds to the pixels with charges. Its slope depends on the applied EM gain. The camera output can be modelled as a convolution of the readout noise Gaussian $\mathcal{G}(\sigma_{\text{read}})$, centered at some baseline b, with the distributions of secondary electrons x created by the EM gain register from n primary electrons (eq. 3.1) as

$$S(x) = (\mathcal{G}(\sigma_{\text{read}}) * (p_0\delta + \sum_{n=1}^{\infty} p_n P_n)(x-b)\ . \tag{3.2}$$

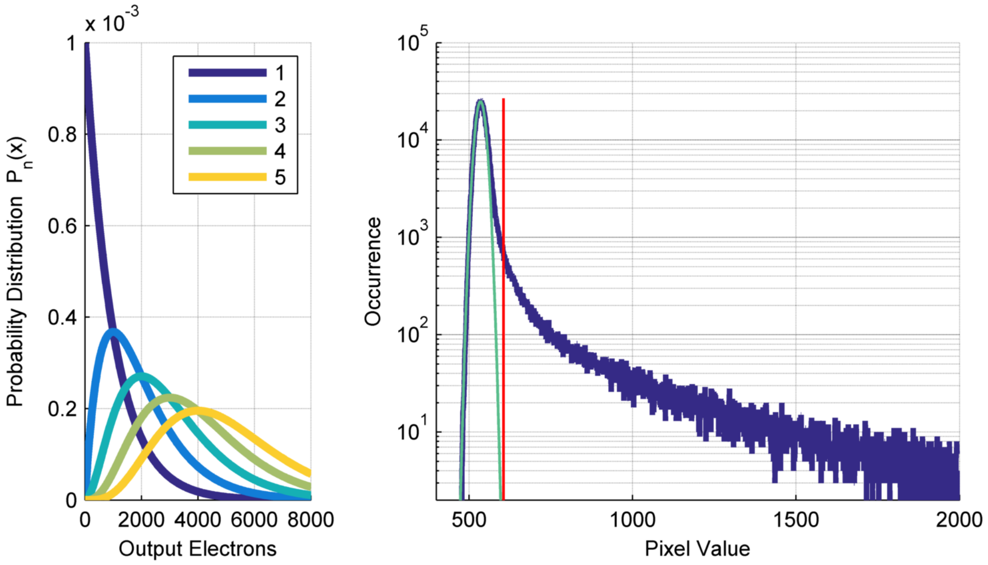

FIGURE 3.3. **Probability Distributions for the EM Gain Register Output. Left:** Probability distributions for $n = 1, 2, 3, 4, 5$ input electrons and gain $g = 1000$. As the distributions overlap substantially it is impossible to deduce the initial number of input electrons from the EM register output electrons. **Right:** Typical histogram of a dark image (taken with camera shutter closed) on logarithmic scale. The readout noise is obtained from a Gaussian fit (in green) to the peak corresponding to the empty pixels. The cutoff (in red) in this example is then set to $5\,\sigma_{\text{read}}$.

Here, p_n is the amount of a pixels having n primary electrons. When it comes to distinguishing empty pixels from those with charges, its the most difficult to tell apart empty pixels from those with one primary electron. An ideal cutoff value minimizes the probability to falsely identify readout noise as signal from one electron, $P(0 \longrightarrow 1)$, while also minimizing the probability $P(1 \longrightarrow 0)$ to overlook a solitary electron.

In a regime where we expect either zero or one electrons on each pixel, the camera output can be modelled as

$$S(x) = (\mathcal{G}(\sigma_{\text{read}}) * (p_0\delta + p_1 P_1))(x - b) \ . \tag{3.3}$$

The probability $P(0 \longrightarrow 1)$ can be calculated by integrating over the Gaussian distribution of the readout noise from a cutoff to infinity:

$$\mathscr{P}(0 \longrightarrow 1) = \int_{\text{cutoff}}^{\infty} \frac{1}{\sqrt{2\pi}\sigma_{\text{read}}} \, \mathrm{e}^{\frac{-x^2}{2\sigma_{\text{read}}}} \, \mathrm{d}x \tag{3.4}$$

The probability that a single electron is not amplified above the cutoff can be calculated by integrating over the probability distribution of the EM register's output eq. 3.4 up to the cutoff value:

$$\mathscr{P}(1 \longrightarrow 0) = \int_{0}^{\text{cutoff}} \frac{1}{g} \, \mathrm{e}^{\frac{-x}{g}} \, \mathrm{d}x = 1 - \mathrm{e}^{\frac{-\text{cutoff}}{g}} \tag{3.5}$$

As will be discussed in section 4.4.2, for our standard imaging parameters the readout noise of our camera typically is $\sigma_{\text{read}} \approx 22.5\,\mathrm{e}^-$, while the real EM gain is typically $g \approx 310$, as will be discussed in section 4.4.3. Thus, for a cutoff of $3\,\sigma_{\text{read}} = 3 \cdot 22.5\,\mathrm{e}^-$, the probability to set a pixel with a single charge to zero is $\mathscr{P}(1 \longrightarrow 0) = 20.2\,\%$, while the probability to identify an empty pixel as one with charge is $\mathscr{P}(0 \longrightarrow 1) = 0.13\,\%$. For $5\,\sigma_{\text{read}}$, the probabilities are $\mathscr{P}(1 \longrightarrow 0) = 31.3\,\%$ and $\mathscr{P}(0 \longrightarrow 1) = 2.87 \cdot 10^{-5}\,\%$.

Figure 3.4 shows examples of simulated single atom signatures and their binarized signals for

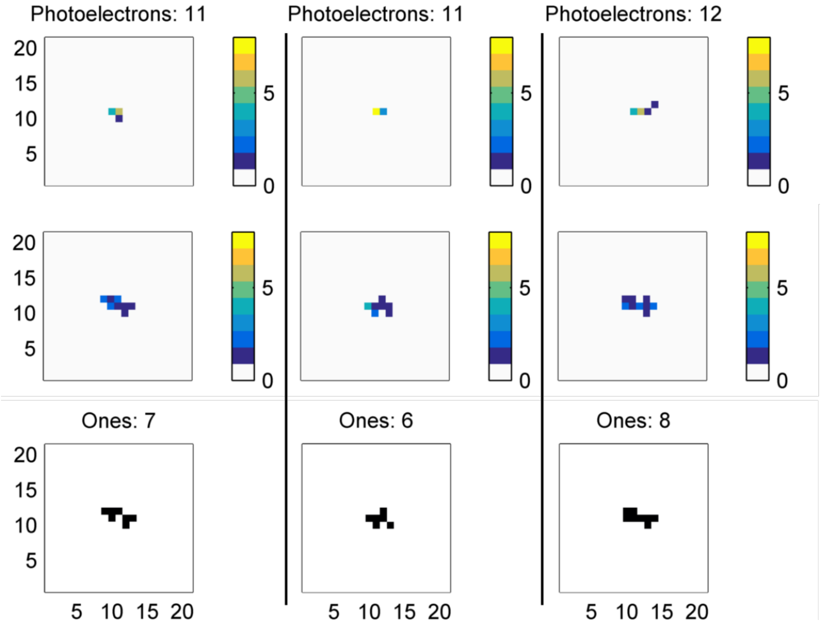

FIGURE 3.4. **Examples of Binarized Single Atom Signals. Top Row:** The atoms diffusion as well as scattered and collected photons are simulated for an imaging duration of 10 μs. **Middle Row:** To include the influence of imaging aberrations, each created photoelectron is redistributed according to probabilities given by the PSF. **Bottom Row:** The single atom signals are binarized according to probabilities for $g = 310$ and a cutoff of $5\,\sigma_{\text{read}}$.

an imaging duration of 10 μs. In the top row, photoelectron distributions are simulated as described in section 2.3.3. Then each photoelectron is redistributed according to probabilities given by the point spread function as discussed in section 2.3.4. Eventually the signal is binarized according to $g = 310$ and a cutoff of $5\,\sigma_{\text{read}}$. To include the binarization in the simulation a random number ($\in [0, 1]$) is drawn for each pixel, deciding whether or not its photoelectrons are amplified above the cutoff. For example, for our parameters the probability to set a pixel with one initial electron to on is 69 %. The pixel will be set to on if the drawn number is below 0.69, otherwise it will be set to off. The probabilities for other amounts of initial electrons can be calculated as in eq. 3.4 and eq. 3.5 by integrating over the corresponding EM register output given by eq. 3.1.

To get a feeling for the effect of binarization on the atom's signal, simulated signals are binarized. Individual realizations of simulated atom signals can only give an impression of what the signals can look like. For a more general idea we have to include many runs of the simulation. 5000 single atom signals were simulated for imaging durations of $10, 15, 20, 30\,\mu$s ($g = 310$, cutoff$= 6.5\,\sigma_{\text{read}}$[1]), and the number of created photoelectrons and the number of pixel set to on in the binarized signals counted. Also, in order to determine a strategy to find single atoms on a (noisy) picture, it will be relevant how these pixels are distributed. It will be especially interesting if the on-pixel are all connected as next neighbours, or if they form multiple unconnected regions. Therefore the number of clusters as well as their size are extracted as well. The results can be seen in fig. 3.5.

We find that the mean number of created photoelectrons is consistent with the analytical estimation in section 2.2 of 11.6 photoelectrons$/10\,\mu$s. The ratio of created photoelectrons and on-pixels per single atom depends on the EM gain and cutoff used, but also on the motion of the atom and over how many pixels the photoelectrons are distributed. For 10 μs imaging it is very likely that the pixel set to on form a single cluster. The longer the imaging duration, the more likely it is that multiple clusters are created. Notably common are single unconnected ones. These will be particularly disadvantageous when it comes to distinguishing signal from noise or one atom signal from another.

---

[1] For comparability, because this cutoff is later used on experimental data.

Not included in this simulation is the noise, knowledge about which is indispensable when choosing a method to identify atoms on the images. The noise in our system will be investigated in the next chapter.

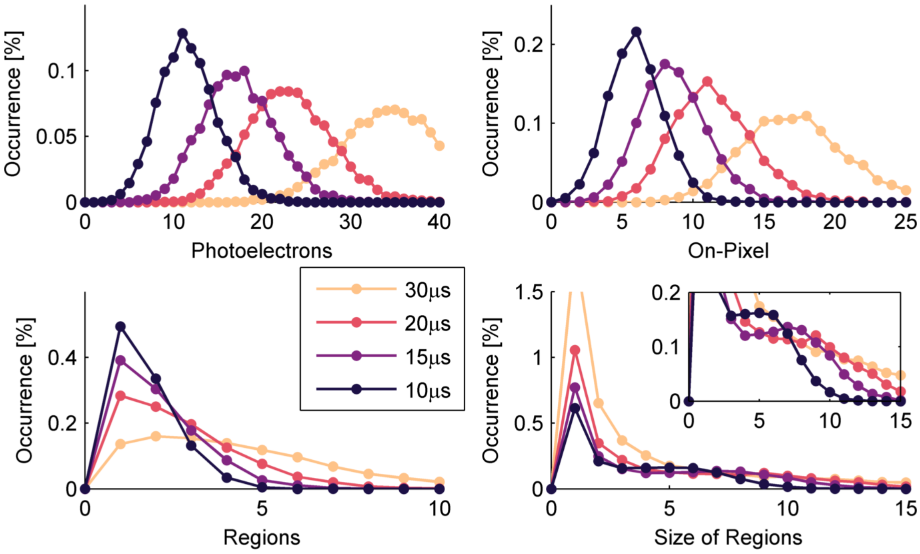

FIGURE 3.5. **Statistical Overview over Simulated Single Atom Signals.** 5000 runs were simulated with $g = 310$ and cutoff$= 6.5\,\sigma_{\text{read}}$ for several imaging durations. **Upper Left:** Amount of created photoelectrons per signal. From the analytical calculations we expect 11.6 photoelectrons/10 μs. **Upper Right:** Number of on-pixels per binarized signal. **Lower Left:** Number of unconnected clusters of on-pixels per signal. **Lower Right:** Size of the individual regions per signal. Single unconnected ones are very common, which is unfavorable when it comes to identifying individual atoms.

4 Experimental Setup

In this chapter, the experiment and its imaging setup are described. Then, the performance of the EM CCD camera is investigated in terms of noise sources and effective gain. Eventually, the influence of different stray light sources is measured.

4.1 The BECK Experiment

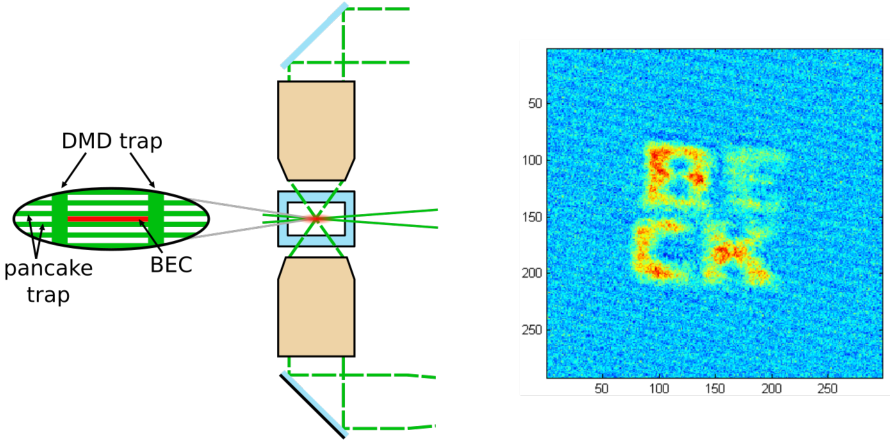

FIGURE 4.1. **Confinement of the 2D BEC. Left:** The pancake trap hold the BEC tightly confined in the gravitational direction and creates its 2D shape. Radial confinement is provided by potential walls created by the DMD. Because the DMD can create (almost) arbitrarily shaped potential walls, the atomic cloud can be brought into various shapes. **Right:** One of the various shapes the BEC can be brought into.

This thesis has been conducted at the BECK experiment, which is based on a 2D potassium BEC. To prepare the BEC, thermal potassium atoms from an oven are first trapped and pre-cooled into a 2D magneto-optical trap (MOT). The 2D MOT creates an atomic beam which is used to load a 3D MOT in the experimental chamber. After a short phase of compressed MOT the atom cloud is loaded into a grey molasses [27, 28], from where the atoms are transferred briefly into a magnetic trap that only traps atoms in the desired state ($\big|F, m_F\big\rangle = \big|1, -1\big\rangle$ at low magnetic fields). Next the cloud is loaded into an attractive optical dipole trap, created by overlapping the foci of two laser beams. In this trap, the atoms are cooled further via evaporative cooling and condense into a BEC. To achieve the 2D shape the BEC is transferred into another dipole trap, the so-called pancake trap. It consists of horizontal sheets of light with a spacing of $5\,\mu$m, which are created by interfering two laser beams under an angle of $6\,^\circ$ as sketched in fig. 4.1. The atom cloud is loaded into one of these sheets (or pancakes), giving it its 2D shape. Radial confinement is added by a Digital Mirror Device (DMD) that allows to create dipole traps of various depths and shapes. The atom number of the 2D BEC is typically on the order of 20.000. For the repulsive dipole traps light with a wavelength of 532 nm is used. This preparation of the experiment's initial state takes approximately 19 s. For more detail on the preparation of the BEC and the BECK experiment in general see [29].

4.2 Imaging Setup

Of the many cameras built into the BECK experiment, two can be used to observe the 2D BEC. One camera ("Pixis") is pointed at the BEC from the side and is used for adjustments, e. g. to ensure that the atom cloud is indeed only loaded into one of the pancake traps. The main camera ("ProEM") of the experiment looks onto the BEC from below. Both these cameras were set up to take absorption images, therefore their respective imaging lights point at the cameras through the atom cloud. To take fluorescence images with the main camera, we use the imaging light of the Pixis camera to illuminate the atom cloud from the side whilst the main camera collects the fluorescence from below.
The imaging systems main components are two identical objectives (NA = 0.5, back-focal length 35 mm). One is installed above the experimental chamber, one below. A sketch of the imaging setup can be seen in fig. 4.2. For absorption imaging only the bottom objective is necessary. Its focus lies in the atom plane, and together with a secondary lens it images the atoms onto the camera. Since for absorption imaging the atoms are illuminated from above and thus the imaging light has to pass the upper objective, additional lenses are used to achieve a collimated imaging beam in the atom plane. The upper objective is required to focus light coming from the DMD into the atom plane. Since the DMD light will pass the experimental chamber and will be imaged onto the camera just like the imaging light, a dichroic mirror (Thorlabs DMLP650L, [30]) and two optical filters (Single-Band Bandpass Filter Semrock FF01-766/13-25 [31] and Single Notch Filter AHF F40-534 [32]) are placed in front of the camera to reduce the influence of all wavelengths other than 767 nm.
For fluorescence imaging the atom cloud is illuminated from the side with linearly polarized light. The two imaging transitions employed in our imaging scheme are driven by σ^+- and σ^--polarized light coming from above (compare section 2.1.3). When illuminating the atoms from the side this could be reproduced using horizontal polarization. This effectively reduces the intensity the atoms experience by a factor of 1/2.. The imaging light has to come from two opposing directions to reduce the atom's diffusion during the imaging process, which is realized by retro-reflecting the imaging light using a mirror behind the experimental chamber. With horizontally polarized light the back-reflected light would interfere with the incoming light, creating an non-homogeneous intensity. To avoid this, the incoming imaging light is linearly polarized but rotated by 45 ° against the horizontal, which again reduces the effective intensity of one beam by a factor of 1/2. A quarter-wave plate placed in front of the retro-reflection mirror rotates the polarization such that the polarization of incoming and outgoing light are perpendicular. The imaging pulse duration is set by the experiment control, for absorption imaging the pulse duration is typically 10 μs. The atom's fluorescence signals are collected by the bottom objective and imaged onto the camera.

4.3 Camera ProEM HS:1024BX3

The BECK experiment's main camera is the EM CCD camera ProEM HS:1024BX3 by Teledyne Princeton Instruments. The image array of the CCD chip consists of 1024^2 pixels with a pixel size of $(13\,\mu\mathrm{m})^2$ and is back-illuminated. For technical specifications of the camera see table 4.1.
A sketch of the camera's internal structure can be seen in fig. 4.3. Images can either be read out using a traditional readout register, or using a EM gain register. To allow higher frame rates the camera can be operated in frame transfer mode. The cameras' CCD chip consists

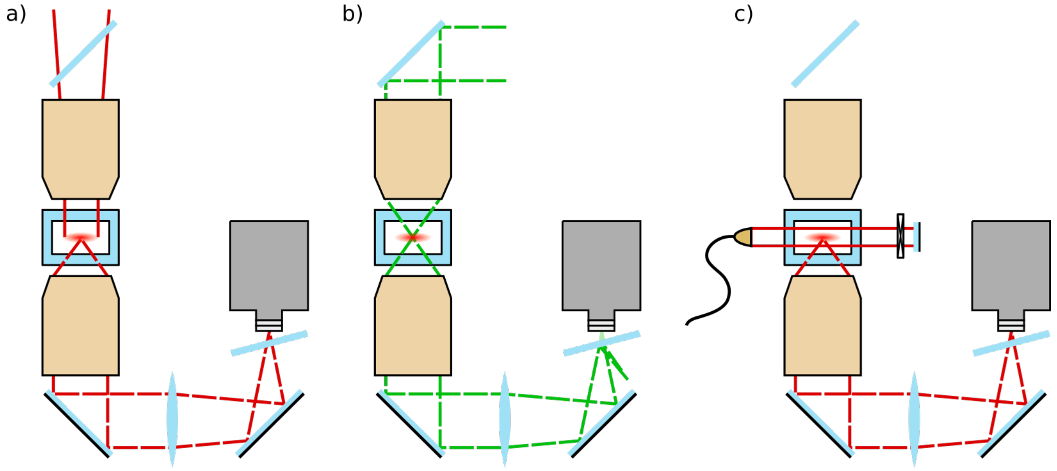

FIGURE 4.2. **Imaging Setup for the DMD, Absorption and Fluorescence Imaging.** Solid lines indicate beam profiles, dashed lines depict the path of rays coming from a point source. The main components of the setup are two identical objectives placed above and below the experimental chamber. **a)** For absorption imaging the atom cloud is illuminated from above. A secondary lens is used behind the lower objective to image the atoms onto the experiment's main camera. **b)** The top objective focuses the light coming from the DMD into the atom plane. A dichroic mirror and two optical filters are placed in front of the camera to reduce noise from DMD light. **c)** For fluorescence imaging the atoms are illuminated from two opposing sides. For this the incoming beam is retro-reflected by a mirror placed behind the experimental chamber. To avoid interference effects a quarter-wave plate rotates the polarization of the back-reflected light by 90 ° against the incoming linearly polarized light.

of 1024×2048 pixels of which only one half, the image array, can be illuminated. After the exposure time the image is shifted from the image array onto the storage array, from where it is then is read out. Because shifting the image takes less time than the readout, which takes approximately 230 ms, the imaging array is cleared quicker and a second image can be taken immediately. This is especially useful for applications were e. g. a reference image has to be taken. Nonetheless, the frame rate can never be quicker than the rate at which images can be read out, since the storage array has to be emptied before shifting another picture. The standard method to take an image at the BECK experiment is the following. First, the CCD chip has to be cleared of the charges that accumulated since the last picture was taken. This is done by shifting the charges onto the storage array and reading them out. Simultaneously the image is taken with an exposure time of 1 ms. However, this image has to remain on the imaging array until the storage array is cleared, that is until the storage array is read out. Therefore, after the image is taken, it remains on the imaging array for 229 ms before it is shifted and read out in another 230 ms.

4.4 Characterizing Camera Performance

To characterize the cameras performance the noise sources (discussed in section 3.2) are measured on our imaging setup and the technical noise is compared to the specifications given by Teledyne Princeton Instruments. Some camera specifications were determined by the manufacturer for our camera specifically. However, since they were mostly determined for non-EM pictures, they were measured differently and are not necessarily transferable to

	Teledyne ProEM HS:1024BX3
CCD Array Size	$1024 \times 1024\,\mathrm{px}$
Pixel Size	$(13\,\mu\mathrm{m})^2$
Dark Current @ $-55°$ C	$0.0098\,\mathrm{e}^-/\mathrm{px}/\mathrm{s}$
EM Gain	1x–1000x
Clock-Induced Charges	$\leq 0.02\,\mathrm{e}^-/\mathrm{px}/\mathrm{frame}$
Vertical Shift Speeds	$0.7\,\mu\mathrm{s}$ - $5\,\mu\mathrm{s}$
Readout Rates	5 MHz, 10 MHz, 20 MHz, 30 MHz
Readout Noise (rms) @ 5 MHz	$19.7\,\mathrm{e}^-$
Conversion Gain (setting "high")	$1.61\,\mathrm{e}^-/\mathrm{cts}$

TABLE 4.1. **Camera Specifications in EM Mode as given by the Manufacturer.** Taken from appendix A.1.1 and appendix A.1.2. Dark Current, Readout Noise and Conversion Gain were measured by the manufacturer specifically for this camera.

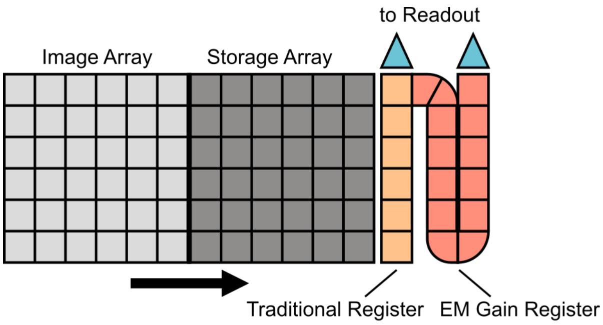

FIGURE 4.3. **Internal Structure of a Frame Transfer EM CCD Camera.** The image can be read out either by using a traditional readout register, or using the EM gain register to multiply the charges. To achieve higher frame rates the camera can operate in a frame transfer mode: The image is quickly shifted from the image array to the storage array, from where it is then read out. Thus the image array is emptied quicker and another image can be taken sooner.

our camera settings. For the manufacturer's test protocol see [33].

The influence of the different technical noise sources depends on various parameters like readout and shift speeds, integration time, temperature and whether or not the camera is operated in EM mode. This makes it hard to exactly quantify the influence of the different sources. Distinguishing thermal from clock induced charges for instance can only be done by measuring at specific camera parameters for which one of the noise sources can be neglected. However, since the noise can depend on the camera parameters, the result of the measurement is not necessarily transferable to the camera settings we actually use. Additionally, the technical noise on CCD chips is not evenly distributed. Each CCD chip has its own "dark noise pattern", because e.g. the thermal current slightly varies from pixel to pixel. Therefore the noise specifications as measured by the manufacturer can be used as a first measure to assess the camera, but we have to investigate the technical noise for our camera settings specifically.

To reveal the technical noise pattern of our camera, images were taken with typical settings[1] and the camera shutter closed. The images were stored on the camera chip for 7 s before readout to let dark charges accumulate. Then a mean image was calculated, which can be seen in fig. 4.4. The images are read out towards the top, such that the upper rows are read out first. The dark noise pattern reveals a prominent frame on the edges of the CCD array where the pixels accumulate dark counts quicker. Additionally, one can see a triangular area on the right side of the array that also exhibits more dark counts.

---

[1] $g = 310$, $T = -65\,°\mathrm{C}$, $\mathrm{VSS} = 0.7\,\mu\mathrm{s}$

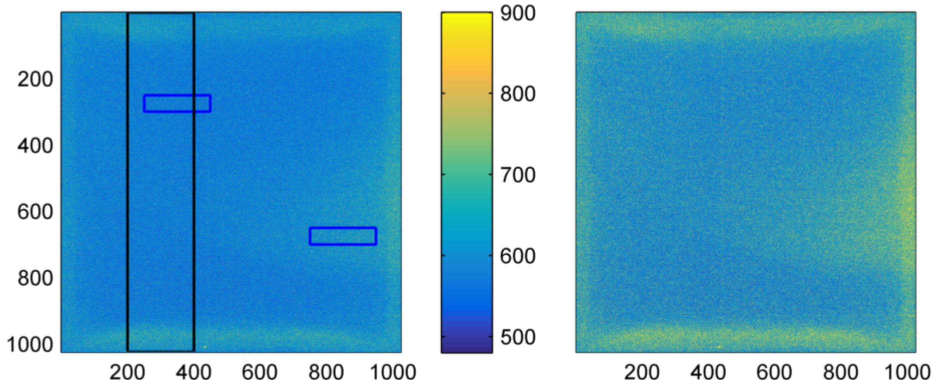

FIGURE 4.4. **Dark Noise Pattern of the Camera's CCD Chip.** Mean over 40 dark frames, each stored on the CCD chip for 3 s before readout. In the right image the colorbar was adjusted to accentuate the pattern. The images are read out towards the top. Since the amount of dark charges is so non-homogeneous, the dark current will be evaluated separately for the areas in the blue boxes. The area in the black box will be used to illustrate the noise dependence on row number.

4.4.1 Thermal Counts and Clock-Induced Charges

The dark current is not identical for all pixels and the pattern of the dark noise is determined by the manufacturing. To reduce the influence of thermally produced charges we operate the camera at its lowest temperature setting, which is $-65\,°\mathrm{C}$. The camera manufacturer specified a dark current of $0.0098\,\mathrm{e}^-/\mathrm{pix/s}$ at a temperature of $-55\,°\mathrm{C}$, which probably was measured as described in [33] for non-EM operation.

To get an estimation of the thermal current to compare with the manufacturers measurement, dark images were taken (with camera shutter closed) for different integration times ($g_{\mathrm{set}} = 1000$, $\mathrm{T} = -65°\mathrm{C}$, 25 shots each). The images were kept on the image array for up to 5 s before readout. Then the regions outlined in blue in fig. 4.4, left of each image were binarized with a cutoff of $3\,\sigma_{\mathrm{read}}$. The ratio of pixels set to on / pixels in the region is plotted against integration time in fig. 4.5, left. Using a linear fit we extract the rates at which dark counts are created. This method of estimating the dark current is accurate only as long as no more than one thermal electron is collected per pixel. For comparably long integration times the probability rises to have several thermal electrons per pixel, which however will only be counted as one because of the binarization, underestimating the dark current for longer integration times.

We find a dark current of

$$(0.0477 \pm 0.0022)\,\mathrm{counts/px/s} \equiv (0.0768 \pm 0.0035)\,\mathrm{e}^-/\mathrm{px/s} \tag{4.1}$$

in the upper box, which is almost a factor of 8 larger than the manufacturers measurement, and

$$(0.0667 \pm 0.0028)\,\mathrm{counts/px/s} \equiv (0.1074 \pm 0.0045)\,\mathrm{e}^-/\mathrm{px/s} \tag{4.2}$$

in the lower box, which is larger by almost a factor of 11.

For our typical exposure time of 1 ms this dark current would create on average merely 50 or

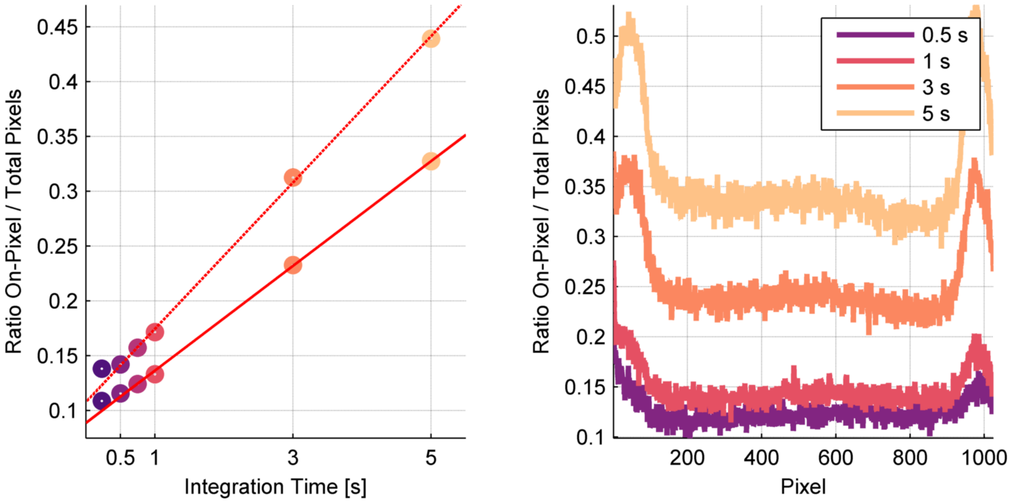

FIGURE 4.5. **Estimation of the Camera's Dark Current and CICs. Left:** Dark images ($g_{\text{set}} = 1000$, $T = -65°\text{C}$) were taken for different integration times and the areas marked by the blue boxes in fig. 4.4 binarized with a cutoff of $3\,\sigma_{\text{read}}$. The lower set of data points belongs to the upper box. A linear fit gives the dark currents. **Right:** Ratio of pixels set to on per row in the area marked by the black box in fig. 4.4 for different integration times. Row 1 is the first to be read out, row 1024 the last.

70 thermal counts on the full camera chip, respectively. The readout of the whole camera chip however takes around 230 ms, during which dark counts also accumulate. The row that is read out first will be affected the least, the last row will have accumulated thermal counts for another 230 ms. This effect is mixed with clock induced charges that are also mostly created on the rows furthest from the readout register, making it impossible to distinguish the two influences quantitatively. The dependence of the noise on the row number is shown in fig. 4.5, right. In the dark images the area marked with the black box in fig. 4.4 was binarized, again with cutoff $3\,\sigma_{\text{read}}$. Then the number of pixels set to on per row were determined and the mean ratio of pixel set to on plotted. Again one can see the peaks at the edges of the chip that correspond to the bright frame of the dark noise pattern. After the peak the amount of noise charges increases slightly with increasing row number as expected because of dark counts and CICs, until they suddenly decrease again.

In the typical imaging procedure described above (clearing the chip by reading it out, then taking the image) the image remains on the imaging array for additional 230 ms because the storage array is not cleared yet. This drastically increases the amount of thermal charges that accumulate. To circumvent this the camera has a cleaning function. Once the cleaning mode is triggered, the rows of the CCD chip are continuously shifted downwards towards the readout to clear them of spurious charges. Another trigger stops the cleaning and an image is taken, which is shifted immediately onto the storage array and read out. Operating the camera in this mode thus reduced the influence of thermal noise. However, because the rows are shifted quickly, the influence of CICs can be increased. Also, if the cleaning runs too long it heats up the CCD sensor.

The camera's dark noise pattern when operated with cleaning can be seen in fig. 4.6, left. The pattern was measured in the same way as the pattern of the standard imaging method. The amount of dark counts is reduced drastically and the dark pattern is much less prominent. On the right of fig. 4.6 again the dependence of pixels set to on (and hence of the noise) on the row number is shown. After 3 s, the mean amount of pixel set to on is only about 1/3 as high as on the uncleaned pictures. Therefore the camera is operated in cleaning mode for fluorescence imaging.

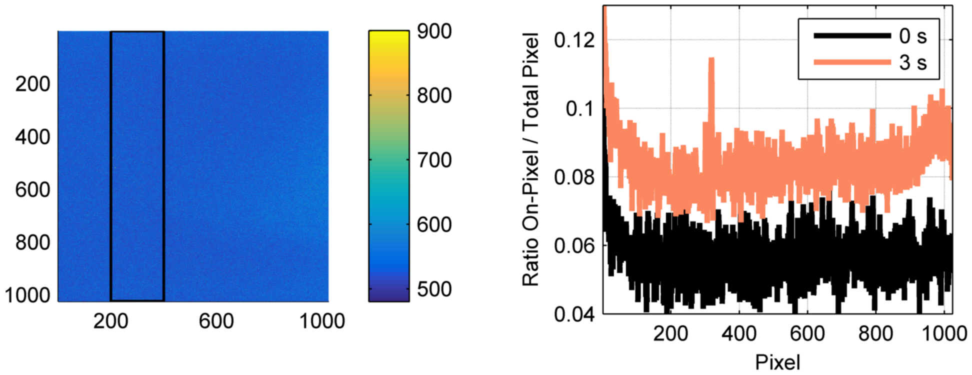

FIGURE 4.6. **Dark Noise Pattern of the Camera's CCD Chip with Cleaning. Left:** Dark pattern of the camera's CCD chip when operated in cleaning mode. The colorbar is the same as in fig. 4.4, left for comparison. The images were kept on the chip for 3 s before readout. The noise pattern is less prominent compared to the pattern created by the standard imaging method without cleaning. **Right:** Ratio of pixel set to on per row in the area marked by the black box on the left for different integration times. Row 1 is the first to be read out, row 1024 the last.

4.4.2 Readout Noise

The readout noise can be extracted from the histogram of any EM CCD image taken in low-photon conditions, for example the dark image depicted in fig. 3.3. By fitting a Gaussian to the peak corresponding to the empty pixels we can identify the readout noise as the width σ_{read} of the Gaussian (compare section 3.4). To minimize the readout noise we always use the lowest readout rate available in EM mode, which is 5 MHz. For this setting we typically find a readout noise of $\sigma_{\text{read}} \approx 14\,\text{cts}$. The conversion gain of the analogue-digital converter for 5 MHz ADC speed when set to high is $1.61\,\text{e}^-/\text{cts}$ (see table 4.1). Therefore our readout noise given in electrons calculates to

$$\sigma_{\text{read}} \approx 14\,\text{cts} \cdot 1.61\,\text{e}^-/\text{cts} \approx 22.5\,\text{e}^- \ . \tag{4.3}$$

This is comparable to the readout noise measured by Teledyne for the same parameters of $19.70\,\text{e}^-$.

4.4.3 Real Gain

The EM gain of a EM CCD camera is controlled via its software. For our camera, the software gain g_{set} can be set to values between 1× and 1000×. This however is not the real gain the electrons experience. The manufacturer calibrates the camera such that the real gain for software gain of 1000 is twice as high as for a software gain of 500 ('gain linearity'). Because the efficiency of the EM gain heavily depends on temperature[2] ([34], [35]), the real gain differs. Additionally, the efficiency of the EM gain ages over time with intensive use ([36],[37]), and has to be re-calibrated periodically.

Like the readout noise, the real gain can be extracted from the histogram of a low photon condition EM CCD image. The slope of the histogram's exponential tail gives the actual EM gain (compare section 3.4). For our typical camera parameters, software gain $g_{\text{set}} = 1000$ and $T = -65\,°$, we find a real gain of $g = 310$.

---

[2] More efficient for colder chip temperature.

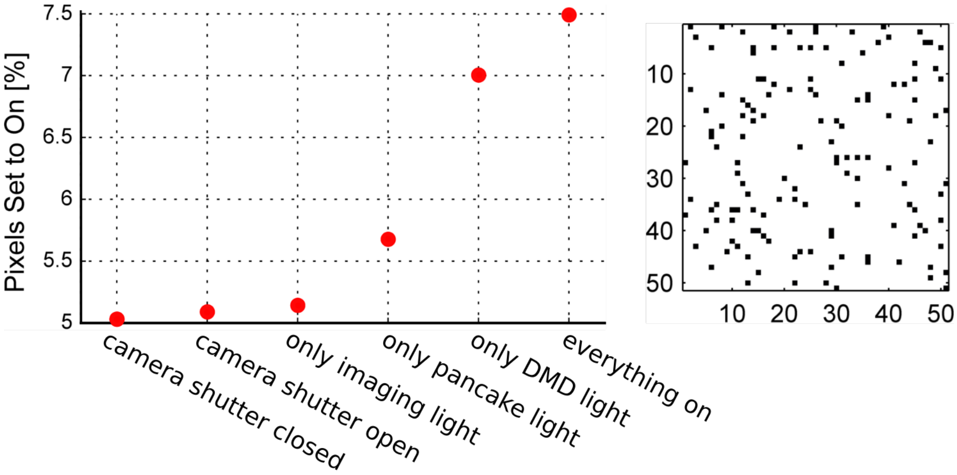

FIGURE 4.7. **Noise from Stray Light Sources. Left:** To compare the influence of the stray light sources, images were taken without any atoms and with different light sources turned on. These were binarized (cutoff $6.5\,\sigma_{\mathrm{read}}$) and compared to images taken with the camera shutter closed. The biggest contribution to the noise makes the DMD, which is turned off right before the images are taken; however, because the camera shutter is opened moments before the imaging pulse, light from the DMD still is collected on the camera sensor. **Right:** Detail of a binarized image where all necessary light sources are turned on, but no atoms are present.

4.4.4 Stray Light

To quantify the influence of stray light on the noise on binarized pictures, images were taken with different light sources turned on (10 pictures each, $g_{\mathrm{set}} = 1000$, with cleaning). The pictures were binarized (without the outer 200 pixels on each edge to avoid the noisy frame of the camera chip) with a cutoff of $6.5\,\sigma_{\mathrm{read}}$ and the percentage of pixels set to on was calculated. The data can be seen in fig. 4.7.

For our camera parameters and with a cutoff of $6.5\,\sigma_{\mathrm{read}}$, the technical noise on the CCD chip results in 5.03 % of the pixels being turned on. When taking fluorescence images the room light is turned off in the lab. Laser light that is not in use during imaging is mostly physically blocked. Several unwanted reflections from laser beams were found that significantly increased noise from stray light, which were then shielded. Overall the stray light from sources that are not necessary for the experiment were minimized. Thus the amount of pixels set to on only slightly increases when the camera shutter is opened and all experimental light sources are blocked.

The retro-reflected imaging beam is oriented perpendicularly to the camera axis and only pulsed on for several microseconds. Therefore it only contributes 0.11 % to the stray light noise for a pulse of $10\,\mu$s. For imaging pulses up to $30\,\mu$s this hardly increases.

A single-band filter is installed in front of the camera that virtually blocks every wavelength other than 767 nm. The repulsive dipole traps (pancakes, DMD) are both created by laser beams with $\lambda = 532\,$nm. To also specifically reduce the influence of light at this wavelength, a single notch filter and a dichroic long-pass mirror are installed in front of the camera (compare section 4.2). The pancake trap is turned on slightly to lightly confine the atoms in the $z-$direction during the imaging process. The pancake beams are rather big and powerful, however they are not aligned with the camera axis but orthogonal to it. Thus the pancakes increase the number of pixels set to on by only 0.65 %.

The biggest contribution to the stray light noise stems from the DMD. The camera shutter has to be fully opened during imaging, which is why the shutter is opened moments before the

imaging light is flashed on. The DMD trap is switched off shortly before the imaging process, and thus the camera also collects some light from the DMD. This produces on average 1.97 % more pixels set to on compared to the case were all light sources were blocked.
Overall, with all light sources that are necessary during imaging, 7.49 % of the pixels will be turned on[3]. This is the noise floor from which the atom signal has to be discerned, which will be discussed in the next chapter.

---

[3] This value is lower than the sum of the contributions, because if several charges are created on the same pixel they will be counted as one.

5 Identifying Single Atoms

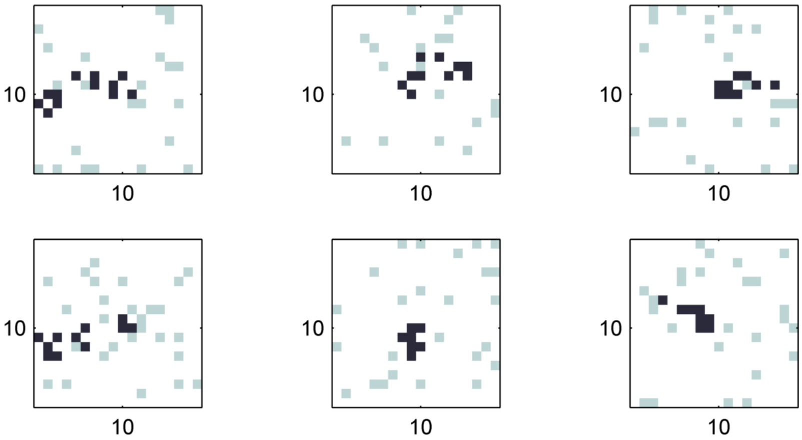

Figure 5.1. **Binarized Simulated Atom Signals in Real Noise Data.** Simulated signals ($20\,\mu$s imaging pulse duration, $g = 310$, cutoff$= 6.5\,\sigma_{\mathrm{read}}$) placed in real noise images.

As discussed in chapter 2, the photons scattered by an atom will not all be collected on one pixel but will be spread over several. Even if the atoms would not move at all during imaging, the PSF would distribute the photons over 3×3 pixels. Since spurious charges are on the same order of magnitude as the atom's signal, charges created not by atoms but by noise will result in similar pixel values. Therefore signal and noise can not be distinguished by pixel value alone, and we have to find other means to tell them apart. While the charges created by noise are (mostly) randomly distributed, the atomic signal shows some bunching, even with the uncertainty introduced by the PSF and the atoms diffusion. As explained in section 3.4, it makes sense to only distinguish between pixels that most likely held charges, which are set to on, and pixels that most likely did not hold charges, which are set to zero. On these binarized images we have to define criteria that indicate atom signal. Examples of simulated atomic signals placed in real noise images can be seen in fig. 5.1. Ideally, a criterion would identify all single-atom signals, while not counting an atom multiple times or falsely identifying noise as atoms.

With our setup, $11.6\,\mathrm{photons}/10\,\mu$s can be collected on average for ideal conditions, as estimated in chapter 2. For simulated data, these result in an average of 6 pixels set to on, often all connected as one big cluster (compare fig. 3.5). However, all these quantities can vary broadly because of the highly stochastic processes involved. During longer imaging durations naturally more signal will be collected. Because of the atom's diffusion however, the added signal will be spread further apart and tends to form multiple clusters. Thus, depending on their identification criteria, detection methods perform differently for different imaging durations.

To find suitable criteria properties are to be investigated for both atomic signal and noise, like e. g. the size of bright clusters. For statistics on the noise a set of empty images is analysed that was taken under typical experimental conditions[1], but without atoms.

---

[1] To avoid the noisy edges of the CCD chip discussed in section 4.4.1, only the inner 774×774 pixels of the

While other experiments have the means to trap individual atoms, the traps of our experiment are designed to confine the entire atom cloud. Single atoms can not be easily prepared with a high fidelity. Therefore the criteria are developed and tested on a set of 10.000 single atom signals simulated as described in section 2.3. The criteria are also applied to the set of empty images to compare the amount of false atoms a technique finds in the spurious charges. Parameters for all images, simulated and measured, are $g = 310$, cutoff $6.5\,\sigma_{\mathrm{read}}$.

5.1 Local Maxima Created by a Low-Pass Filter

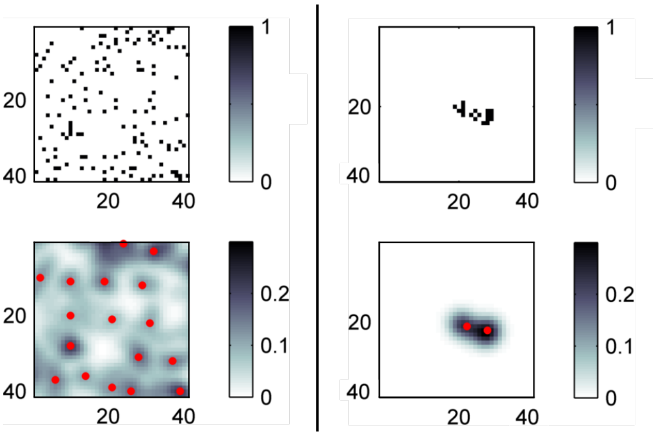

Figure 5.2. **Working Principle of the Low-Pass Filter Method. Left:** Example of an empty binarized image (top) and the same image after a Gaussian filter with a width of 2 pixels was applied (bottom). **Right:** Example of a binarized simulated single atom signal (top, imaging duration $30\,\mu$s), and the signal after the Gaussian filter was applied (bottom). The red dots mark the maxima (pixels with a higher value than the surrounding 8 pixels) of the shape.

To separate random noise from clustered atom signal one approach is to work with a low-pass filter. This method is successfully employed in an experiment of the Group of Prof. Jochim, Heidelberg (see e. g. [38]), where up to two atoms are prepared in dipole traps and imaged either in situ or, for momentum imaging, in free-space after a time-of-flight.

Applying a Gaussian filter to a binarized image results in a picture with values between zero and one. The value of a pixel of the filtered image depends on whether or not it was set to on by the binarization, but also on how many surrounding pixels were turned on. The effect of a pixel on its surroundings depends on the width of the applied filter. The wider the filter, the further reaches the influence of a pixel's value. By filtering an image and then searching for local maxima, we find the "densest point" of a cluster.

Applying this low-pass filter to randomly scattered noise will likewise produce local maxima. Most of these maxima however will have a lower value since the density of the pixels set to on is lower in regions without atoms. Then atom signal can be told apart from noise by the height of the maxima. For this discussion a filter width of 2 pixels was chosen, as it gave the best detection results. Figure 5.2, left shows a region of an empty image binarized (top) and the same region with a filter applied (bottom). In the same figure on the right an example of a binarized (top) and filtered (bottom) simulated single atom signal can be seen. The red dots mark the local maxima.

To determine a value above which the maximum was most likely created by an atom, the set of empty images was analyzed and the values of the local maxima documented. The resulting

---

images were analysed.

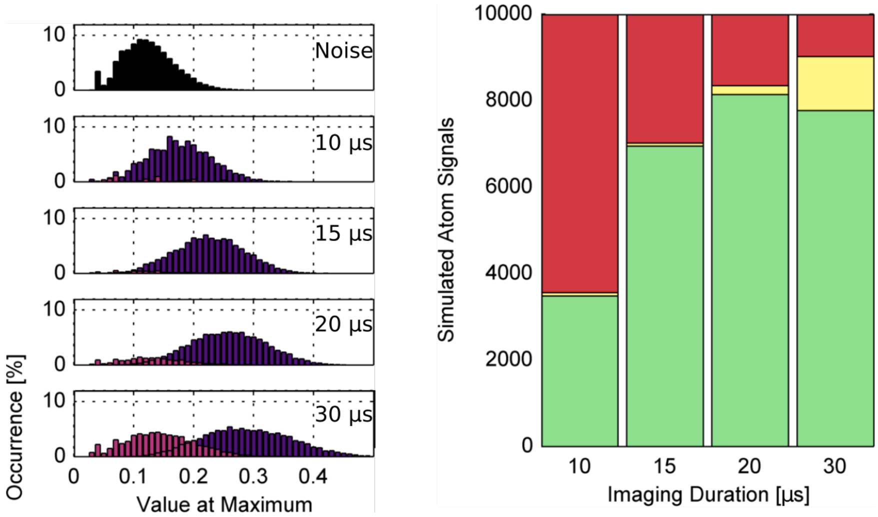

FIGURE 5.3. **Statistics and Performance of the Low-Pass Filter Method. Left:** Histograms of the maxima's values on empty images (top) as well as for simulated single atom signals with different imaging durations (below). The cutoff to identify a maximum as an atom was chosen as 0.2. If a single atom signal creates more than one maximum the highest maximum is included in the purple bars, while the lower maxima are counted in the pink bars. The occurrences are normalized by the number of analyzed simulated atom signals. **Right:** Performance of the technique with a cutoff value of 0.2 on 10.000 analysed simulated single atom signals for different imaging durations. Green marks simulated atoms that have been identified, yellow corresponds to simulated atoms that have been identified but counted more than once because the filtered signal created more than one maximum above the cutoff, and red represents the atom signals that were discarded as noise.

distribution can be seen in the upper histogram in fig. 5.3, left. The distinct peak at 0.04 stems from single pixels set to on that have no surrounding on-pixels within the influence of the filter. The histograms below display the results of the 10.000 simulated single atom signals for the different imaging durations. The distribution for an imaging duration of 10 μs greatly overlaps with that of the empty images. For longer imaging durations higher maxima occur and the overlap with the histogram of the empty images decreases. Consequently, this low-pass filter method performs best for longer imaging durations like 20 μs or 30 μs, and the criterion will be chosen such that it suits this scenario. For longer imaging durations however it also becomes more probable that a single atom produces two local maxima. If both maxima are above the cutoff value, the atom will be counted twice.

We chose a cutoff value of 0.2. On the empty shots, on average 3149 ± 27 local maxima are found per image. With a cutoff of 0.2, 6.4 % of those are falsely identified as atoms, that is 201 ± 17 atoms per 774×774 empty pixels. The criterion's performance on 10.000 analyzed simulated single atom signals can be seen in fig. 5.3, right. For 10 μs imaging duration, 65 % of the simulated atoms were discarded as noise. For 15 μs, 69 % of the simulated atoms were correctly identified, while hardly any counted multiple times. For 20 μs and 30 μs around 80 % of the atoms were detected. Only for the longest simulated imaging duration of 30 μs the effect that one atom is counted as several has a bigger influence, where 9 % of the atoms were counted more than once. However, if the atomic sample to be imaged is homogeneous and of very low density, this effect could be corrected by rejecting atoms that were found especially close together. Choosing a lower cutoff would increase the amount of detected atoms, at the cost of falsely identifying more atoms in the noise.

This detection technique works best for rather long imaging durations, which limits the atomic densities this method can sensibly be used on. If the density is to high and the atomic signals overlap to create one maximum, they will be counted as one atom and thus the atom number will be underestimated. Similarly, if it is likely that two atom signals overlap, counting atoms twice can not be avoided by rejecting atoms that were found close together.

5.2 Size of Clusters

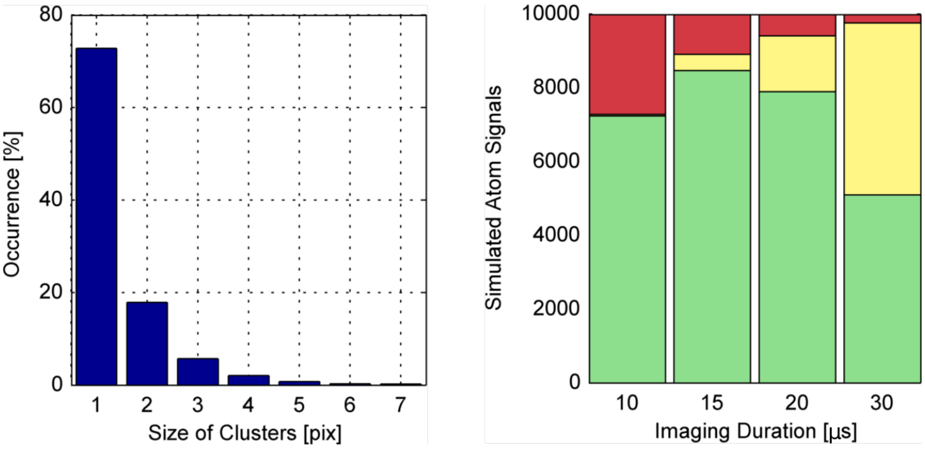

Figure 5.4. **Statistics and Performance of the Cluster Method. Right:** Histogram of the size of clusters found on empty pictures. **Left:** Performance of the method. Clusters that consist of at least 4 pixels are regarded as atoms. Green marks simulated atoms that have been identified, yellow are simulated atoms that have been identified but counted more than once because the signal created more than one cluster of 4 or more pixels, and red are atom signals that were discarded as noise.

In this approach the size of bright clusters of directly connected on-pixels is used as feature to identify atoms. The idea behind this is similar to that of the low-pass filter approach: While atomic signal mostly appears in clusters, noise will hardly produce larger bright regions. A cluster is formed by pixels set to on that are directly connected with each other (as nearest neighbours). Thus a single on-pixel surrounded by pixels set to off is counted as a cluster of size one.
The set of empty images was binarized and the distribution of the cluster's sizes documented. The resulting histogram is shown in fig. 5.4 on the left. On the empty images 14595 ± 154 clusters were found. Of these, 3.6 % have an area of 4 pixels or larger, that is 524 ± 33 clusters (and thus falsely identified atoms) per empty image. Figure 5.4, right shows the performance of the detection method on 10.000 simulated atomic signals, if all clusters that consist of at least 4 pixels are regarded as an atom. The method works best for moderate imaging durations like 15 μs, were 85 % of the atoms are identified correctly, 5 % are counted twice and 11 % are overlooked.
A downside of this detection method is that bright pixels have to be next neighbours of each other to be regarded as one signal. Especially for longer imaging durations it becomes more likely that the bright pixels form several clusters (see again fig. 3.5), and so the amount of atoms counted several times increases substantially. In addition, since clusters of 4 bright pixels also sometimes appear in the noise, the number of "false atoms" is comparatively high. Choosing a higher cutoff, for example counting all clusters with 5 or more pixels, reduces the false counts but will overlook more actual atoms. If a cluster had to fulfill other criteria in addition to the minimal size, the method's performance could be improved.

5.3 Orientation of Clusters

As discussed in section 2.3.3, the atoms perform a random walk in velocity space during imaging that leads to a diffusive motion. Because the atoms are illuminated from two opposing directions, this random walk is not isotropic but leads to a broader variance along the directions of the imaging beams (compare fig. 2.5). Especially for longer imaging times, this preferred orientation of the atomic signals could potentially be used to identify atomic signals.

Again, 10.000 single atom signals were simulated, binarized, and the orientation of the resulting clusters extracted using the *Matlab* built-in function "regionprobs". The results can be seen in fig. 5.5. As in section 5.2, only clusters with an area of at least 4 pixels were taken into account. The angle is measured relative to the images' x-axis. For the simulated atom signals the imaging beams are aligned with the x-axis.

Unfortunately, no distinct signal can be found in the clusters' orientations. The effect of the diffusion's anisotropy is too weak. In addition, the clusters cannot be oriented in any direction. The on-pixels of a cluster can only be arranged in several ways allowing only certain orientations. This is especially the case for smaller clusters. This is why clusters with an orientation of ±45° are notably common for all imaging durations.

The asymmetric atom diffusion can be increased by making one of the counter-propagating imaging beams weaker. However, this would also increase the atom's diffusion and therefore the atom's signal would be connected in clusters less often.

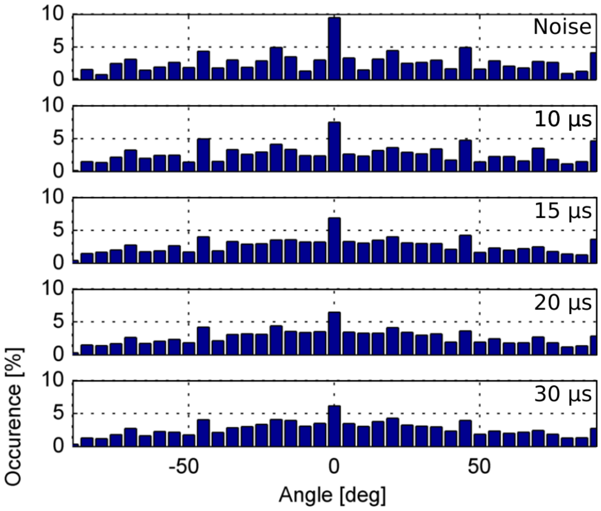

FIGURE 5.5. **Statistics of the Cluster's Orientation.** Empty images as well as 10.000 simulated single atom signals were binarized and the orientation of clusters with an area of at least 4 pixels were extracted. The angle is relative to the x-axis of the images.

5.4 Sum over Pixel Values of Clusters

Another quantity that could distinguish atom signal from noise is the sum over the pixel values of a cluster. The exact number of initial electrons on a pixel can not be deduced from the pixel's value, but pixels with more initial charges will have higher values on average. This can be captured by averaging over the clusters pixel values. This property is not simulated, but directly employed on experimental data in the next chapter.

5.5 Comparison to Experimental Data

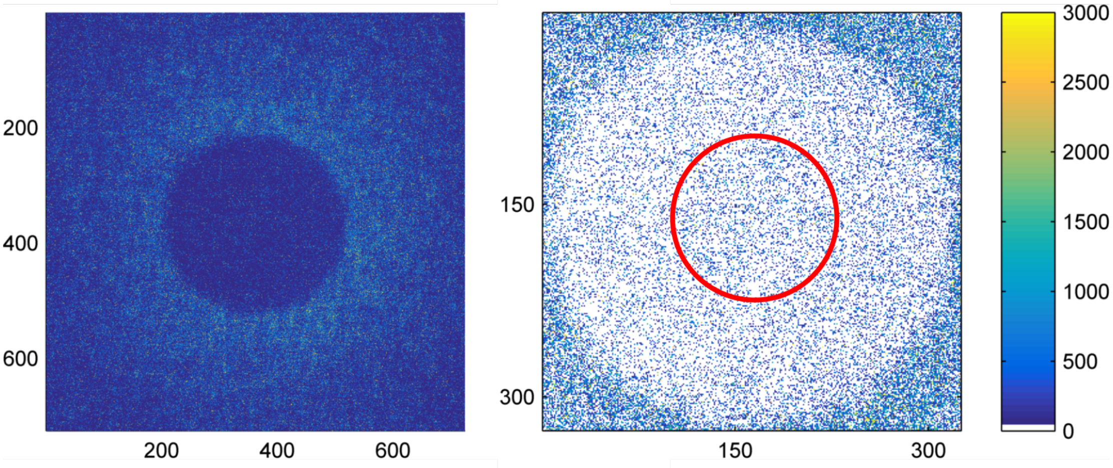

Figure 5.6. **Fluorescence Images of Depleted Densities.** The DMD is used to reduce the density of the BEC by first reducing the radius of the DMD trap, releasing atoms outside of it. Then the trap's radius is slowly increased again to reduce the density inside. **Left:** Example of a raw shot, imaging pulse duration $15\,\mu$s, $g = 310$. **Right:** Binarized image multiplied with the original shot. The area in the red circle is analysed in the following.

The prerequisite for finding single atoms on experimental data is to have suitable experimental conditions, that is having cold, individual atoms. Therefore, to try the detection criteria on experimental data, very dilute densities have to be prepared. These densities cannot be detected with single shots taken with absorption imaging, leaving us without an independent measure of densities and atom numbers. This makes the preparation of suitable densities a trial-and-error task.

In a first approach the DMD was used to decrease the density of the atom cloud as follows. Initially, the BEC is confined in the vertical direction by the pancake trap, while the DMD creates lateral confinement. Then, the radius of the DMD trap is suddenly reduced, releasing the atoms that are now outside of the trap's walls. By slowly increasing the radius of the DMD trap again the atoms outside of the walls are pushed away. Simultaneously, the volume of the trap increases, reducing the density inside. This process can be repeated several times, each time reducing the density further. The resulting density distribution can be seen in fig. 5.6, left. One can clearly see the radius of the DMD trap. Inside the trap the signal is low, while the density is much higher outside due to the atoms that were pushed out of the center.

To test whether or not this procedure results in densities of the right regime, images were taken with imaging pulse durations between $3\,\mu$s and $30\,\mu$s. The images were binarized with a cutoff of $6.5\,\sigma_{\text{read}}$ and for one shot of each imaging duration the clusters of on-pixels were extracted. To compare the images by their cluster sizes and pixel values as proposed in section 5.4 the binarized image was multiplied with the original image, of which an example can be seen in fig. 5.6, right. Then, in a small area in the middle of the trap, the sum over each cluster's pixel values was taken and listed against the cluster's size in pixels in fig. 5.7 for different imaging durations. Images taken under the same experimental conditions but without atoms were treated in the same way for comparison.

For all imaging durations the pictures with atoms exhibit more signal than those without, that is bigger clusters or clusters with higher pixel values. Therefore there must be atomic

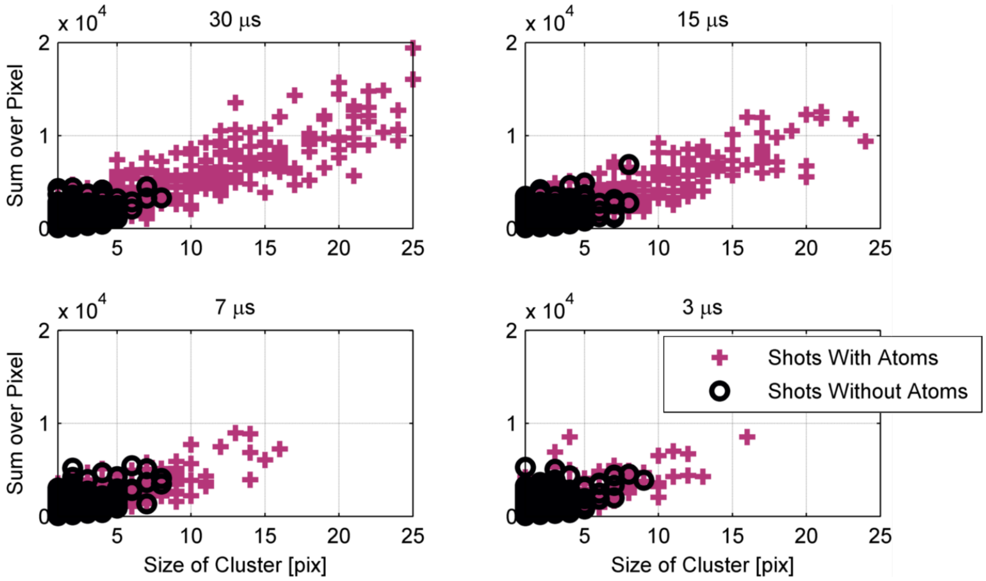

FIGURE 5.7. **Analysis of Experimental Data based on Cluster Sizes and Pixel Values.** For different imaging durations two pictures were binarized, one with atoms and one without. The binarized shots were multiplied with the original image. The size of each cluster and the sum over its raw pixel values were extracted and plotted against each other.

signal in the analysed region. On empty images, clusters rarely have a size greater than 5 pixels. On shots with atoms bigger clusters can be found. However, especially on the shots with longer imaging pulse durations, clusters occur that are too large to contain signal from only one atom. For shorter imaging pulses it is very unlikely that individual atoms scatter enough photons to be detectable. The fact that images with $3\,\mu$s imaging pulse durations also exhibit bigger clusters than empty pictures suggests that these clusters are caused not by individual atoms alone, but either from multiple atoms, or originate from atomic signal together with the background noise. In addition, clusters with sizes between one and four pixels cover a similar range in total signal, as variances for these small sums are high. Thus, noise and atom signal again cannot be clearly separated.

If this method of preparing dilute densities is suitable in general cannot be said from this analysis. The signal found on shots with atoms can stem from cold atoms in the focal plane of the objective, only that the density was too high. The signal can also come from many hot atoms or atoms out of the focal plane, or atoms above each other trapped in different layers of the pancake trap. In both cases the signal of an atom would be spread over a large area, and the signals of the atoms would overlap quickly. If the signal is created by slow atoms in the focal plane, the on-pixels should noticeably form clusters.

To test this, the clusters consisting of four pixels or more are counted in a small area in the middle of the DMD trap. Also, the overall amount of on-pixels in this region is extracted. Then the same amount of pixels is randomly set to on in an area of the same size, and again the clusters of 4 or more pixels are counted. The resulting distributions can be seen in fig. 5.8. Turning on random pixels creates patterns in which the same amount of clusters greater than 4 are found. Moreover, the histograms of cluster sizes look exactly the same (not shown). The signal we collect in the small analyzed region does not bunch more than random noise.

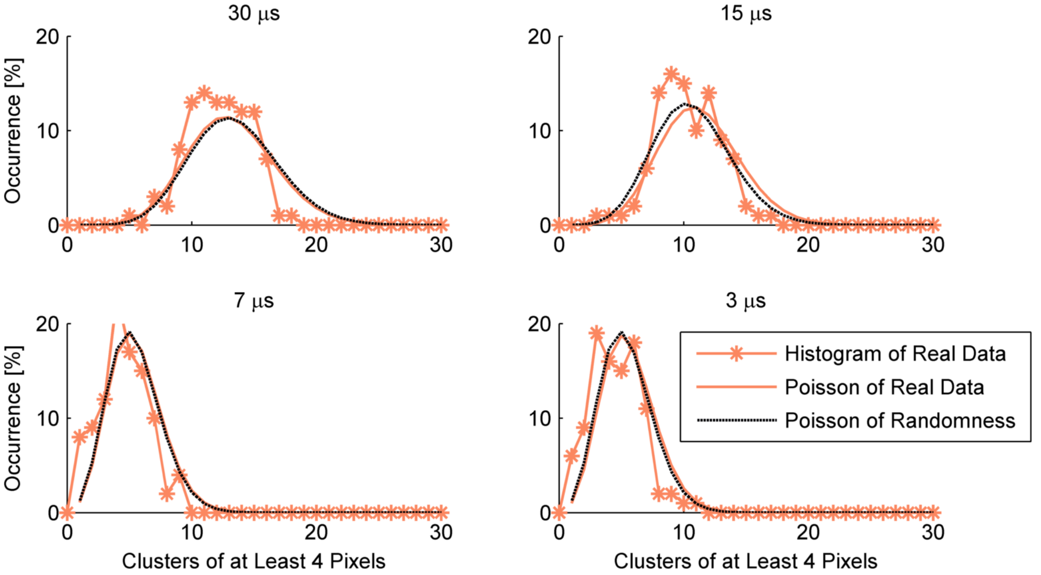

Figure 5.8. **Analysis of Experimental Data Based on Poisson Statistics.** To determine whether the signal on experimental images exhibits bunching, the amount of clusters identified as atoms is documented in a small region of 100 images per imaging duration. The distribution is compared to that extracted in the same way from images were the same amount of pixels was turned on randomly.

5.6 Possible Reasons for Indistinct Experimental Results

So far, no single atom signal could be clearly identified within the experimental data taken, as described in section 5.5. This can have several reasons.

It is probable that the densities were too high. The fact that even for very short imaging durations clusters were found that are unlikely to be caused by one single atom supports this hypothesis.

The observation that the on-pixels do not form more clusters as they would if they were turned on randomly can mean that the atoms are too hot and thus too fast, spreading their signal over a large area without creating distinct bright clusters. It is also possible that the collected signal stems not (only) from the focal plane of the objective, which would lead to a broader effective PSF. This can be the case e. g. if the atoms are not all trapped in the pancake positioned in the focal plane, but some are trapped in the pancakes above or below. Another reason can be that the focus of the imaging system is adjusted based on images taken of the BEC with absorption imaging. For absorption imaging the imaging beams are aligned with the objective, illuminating the BEC from above and thus pushing it downwards, towards the objective. If this displaced the BEC significantly, the focus would be misaligned for fluorescence imaging which does not push the atoms towards the camera.

Also the detection of atomic signal is further impeded by the comparably high noise on the images (compare [39]), caused primarily by the light of the DMD. While clusters of the sizes expected from the simulations for single atom signals were observed, clusters of the same size and with similar or higher pixel value sums were also found in the empty images.

It can be that the imaging intensity was not high enough and fewer photons were scattered per atom than calculated in section 2.2.1. The imaging intensities used were estimated to be a factor of 20 greater than the literature value for the imaging transition's saturation intensity [21]. However, the effective saturation intensity $I_{\text{sat}}^{\text{eff}}$ of the transitions in our experiment depends on the stability of experimental parameters like the magnetic field or the imaging beam's polarization, and can be higher. In [22] it was measured for our absorption imaging that $I_{\mathrm{sat}}^{\mathrm{eff}} = 18 I_{\mathrm{sat}}$. The fluorescence signal could also be weaker than estimated if the NA of the objective is smaller in practise as it is theoretically, which would reduce the percentage of photons that can be collected by the imaging setup.

5.7 Planned Improvements

To get more distinct experimental results, the collected atomic signal has to be increased and the noise reduced. We will redo the measurements with higher imaging intensities and see whether this increases the signal. Furthermore we will investigate the low effective gain of our EM CCD camera, which can probably be improved by re-calibrating the EM gain mode. In addition, the hypothesis that the imaging setup has to be focused differently for fluorescence imaging will be tested. The greatest contribution to the noise on the images stems from stray light of the DMD. Why this is the case, despite the optical filters placed in front of the camera, will also be reviewed.

Furthermore we will look into different methods to prepare appropriately dilute and cold atomic samples. The ability to reliably trap single atoms would allow us to conveniently test our estimation for the signal strengths of single atoms. This could also be used to check if the focus of the imaging system is different for fluorescence and absorption imaging.

To ensure that we prepare in fact single atoms we have to be able to count them. Counting atoms whose signals spatially overlap is possible if the signal strength of different numbers of atoms is sufficiently different. However, the number of photons one atom scatters follows a Poisson distribution $\mathbf{P}(n)$, with n the expected number of photons. The photons collected from N atoms follow the Poisson distribution $\mathbf{P}(N \cdot n)$. Consequently, the longer the imaging duration and thus the higher n, the clearer the separation between the signal strengths. As the width of the Poisson distribution also depends on n, the separation of N and $N+1$ atoms is more distinct for low atom numbers.

This is why we will create very small traps with the DMD and try different methods to load them with small atom numbers to see quantized steps in the signal strength. The stochastic nature of the EM gain will broaden the signal's distribution, increasing the the overlap of the Poisson distributions. Thus, if the noise is low enough, it would be favorable to do this measurements without the EM mode but with longer imaging durations instead.

If single atoms can be prepared reliably and the signal strength of single atoms is known and optimized, the atoms could be released from the traps for the imaging to measure the particle's diffusion. This way the estimations made for the atom's diffusion and could be verified and we knew exactly what signals to expect from freely propagating single atoms.

6 Conclusion & Outlook

In this thesis we investigated the feasibility of fluorescence imaging of freely propagating ^{39}K atoms with single-atom-resolution on our 2D BEC experiment. This capability is interesting for us as we want to measure low populations of momentum modes, which are accessible to us by the technique of phase-space imaging.

We illuminate the BEC with two counter-propagating imaging beams, driving a closed four-level system. To avoid the formation of a standing wave, the polarizations of the imaging beams are oriented perpendicular to another. Photons scattered by the atoms are collected by a high-resolution objective and focused onto an EM CCD camera.
Considering the atoms natural scattering rate and their dipole radiation pattern, as well as the imaging system's transmittance and NA and the camera's QE, we estimate that one atom creates on average 12 photoelectrons per $10\,\mu$s imaging duration. Since the atoms can propagate freely during the imaging process they undergo a diffusive motion, spreading the photoelectrons they create over several pixels. Additionally, the imaging system's PSF further distributes the atom's signal. To estimate the influence of these effects a simulation of single-atom fluorescence signals was developed.

To amplify the faint signals of a few photoelectrons per pixel above the readout noise of the CCD camera we operate the camera in EM mode. The technical noise of the camera was investigated, the camera's performance evaluated and the ideal camera parameters determined. The sources of noise from stray light were investigated and mitigated. The main source of noise remains light from the DMD trap, whose influence is visible despite two optical filters placed in front of the camera.

To distinguish noise from atomic signals different criteria were considered, which are all based on the expectation that charges created by atoms will occur in clusters, while noise will be randomly distributed. The criteria were tested on a set of 10.000 simulated atom signals, where they achieved promising results. Transferring the knowledge gained from simulated single-atom signals to experimental data proofed challenging, as the experimental preparation of suitable densities is a trial-and-error task. So far, the comparison of expectations from simulated signals and experimental data was inconclusive. While the images with atoms exhibit more signal than empty images, this signal is not noticeably clustered. This was concluded from a comparison with randomly generated images.
To improve the experimental results several next steps are planned. Because we have reason to assume that the imaging intensities were too low we will redo the measurements with higher intensity. In addition we want to raise the effective gain of the EM CCD camera by re-calibrating the EM gain mode. To further reduce the noise we will investigate why the DMD trap's influence can still be seen on the camera. To check the assumptions made for the simulation of the single-atom signals we want to develop a method to deterministically trap single atoms.

A Technical Specifcations

A.1 ProEM HS:1024BX3

A.1.1 Excerpts from Data Sheet

For the full data sheet see [36].

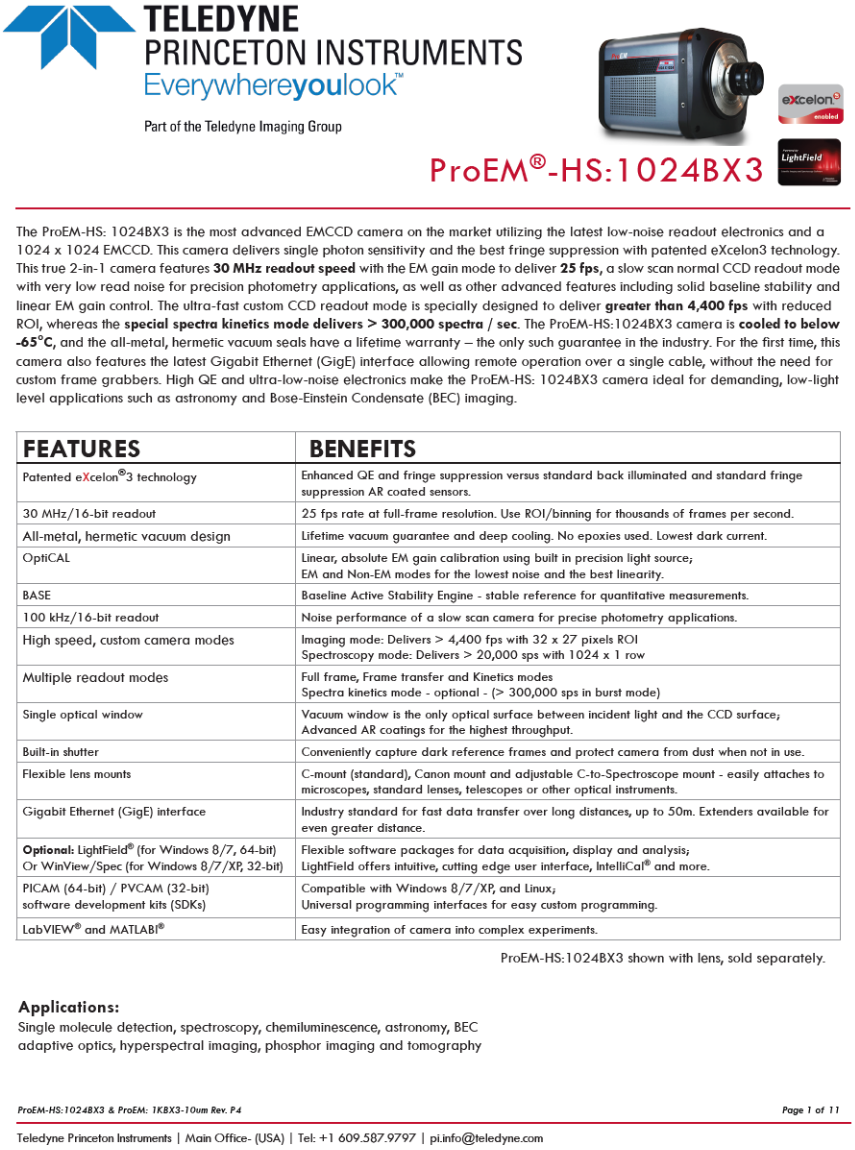

TELEDYNE
PRINCETON INSTRUMENTS
Everywhereyoulook™

Part of the Teledyne Imaging Group

ProEM®-HS:1024BX3

The ProEM-HS: 1024BX3 is the most advanced EMCCD camera on the market utilizing the latest low-noise readout electronics and a 1024 x 1024 EMCCD. This camera delivers single photon sensitivity and the best fringe suppression with patented eXcelon3 technology. This true 2-in-1 camera features **30 MHz readout speed** with the EM gain mode to deliver **25 fps,** a slow scan normal CCD readout mode with very low read noise for precision photometry applications, as well as other advanced features including solid baseline stability and linear EM gain control. The ultra-fast custom CCD readout mode is specially designed to deliver **greater than 4,400 fps** with reduced ROI, whereas the **special spectra kinetics mode delivers > 300,000 spectra / sec**. The ProEM-HS:1024BX3 camera is **cooled to below -65°C,** and the all-metal, hermetic vacuum seals have a lifetime warranty – the only such guarantee in the industry. For the first time, this camera also features the latest Gigabit Ethernet (GigE) interface allowing remote operation over a single cable, without the need for custom frame grabbers. High QE and ultra-low-noise electronics make the ProEM-HS: 1024BX3 camera ideal for demanding, low-light level applications such as astronomy and Bose-Einstein Condensate (BEC) imaging.

FEATURES	BENEFITS
Patented eXcelon®3 technology	Enhanced QE and fringe suppression versus standard back illuminated and standard fringe suppression AR coated sensors.
30 MHz/16-bit readout	25 fps rate at full-frame resolution. Use ROI/binning for thousands of frames per second.
All-metal, hermetic vacuum design	Lifetime vacuum guarantee and deep cooling. No epoxies used. Lowest dark current.
OptiCAL	Linear, absolute EM gain calibration using built in precision light source; EM and Non-EM modes for the lowest noise and the best linearity.
BASE	Baseline Active Stability Engine - stable reference for quantitative measurements.
100 kHz/16-bit readout	Noise performance of a slow scan camera for precise photometry applications.
High speed, custom camera modes	Imaging mode: Delivers > 4,400 fps with 32 x 27 pixels ROI Spectroscopy mode: Delivers > 20,000 sps with 1024 x 1 row
Multiple readout modes	Full frame, Frame transfer and Kinetics modes Spectra kinetics mode - optional - (> 300,000 sps in burst mode)
Single optical window	Vacuum window is the only optical surface between incident light and the CCD surface; Advanced AR coatings for the highest throughput.
Built-in shutter	Conveniently capture dark reference frames and protect camera from dust when not in use.
Flexible lens mounts	C-mount (standard), Canon mount and adjustable C-to-Spectroscope mount - easily attaches to microscopes, standard lenses, telescopes or other optical instruments.
Gigabit Ethernet (GigE) interface	Industry standard for fast data transfer over long distances, up to 50m. Extenders available for even greater distance.
Optional: LightField® (for Windows 8/7, 64-bit) Or WinView/Spec (for Windows 8/7/XP, 32-bit)	Flexible software packages for data acquisition, display and analysis; LightField offers intuitive, cutting edge user interface, IntelliCal® and more.
PICAM (64-bit) / PVCAM (32-bit) software development kits (SDKs)	Compatible with Windows 8/7/XP, and Linux; Universal programming interfaces for easy custom programming.
LabVIEW® and MATLABI®	Easy integration of camera into complex experiments.

ProEM-HS:1024BX3 shown with lens, sold separately.

Applications:
Single molecule detection, spectroscopy, chemiluminescence, astronomy, BEC
adaptive optics, hyperspectral imaging, phosphor imaging and tomography

ProEM-HS:1024BX3 & ProEM: 1KBX3-10um Rev. P4 *Page 1 of 11*

Teledyne Princeton Instruments | Main Office- (USA) | Tel: +1 609.587.9797 | pi.info@teledyne.com

Figure A.1. **Data Sheet, Page 1.**

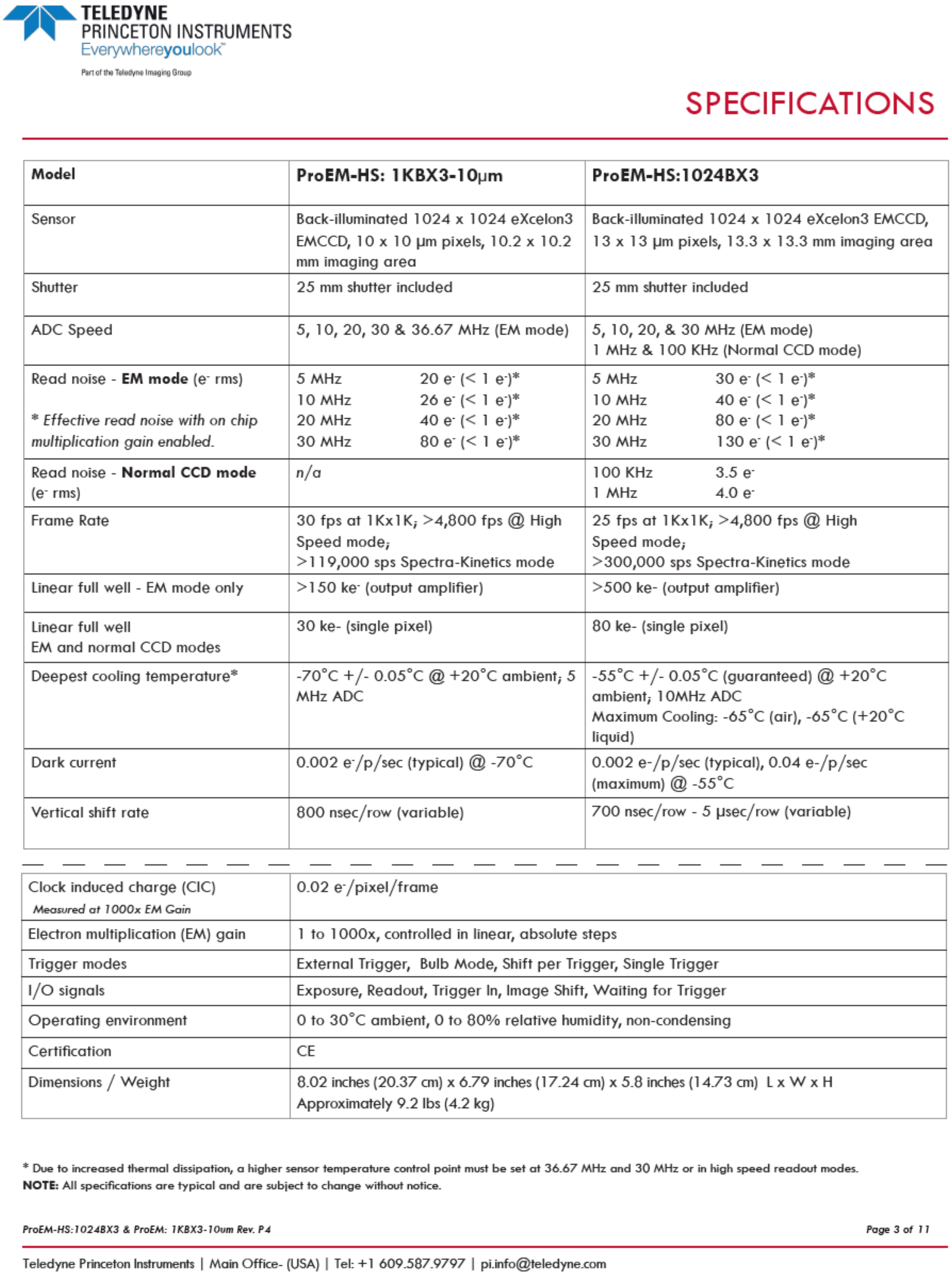

TELEDYNE
PRINCETON INSTRUMENTS
Everywhereyoulook™
Part of the Teledyne Imaging Group

SPECIFICATIONS

Model	**ProEM-HS: 1KBX3-10µm**	**ProEM-HS:1024BX3**
Sensor	Back-illuminated 1024 x 1024 eXcelon3 EMCCD, 10 x 10 µm pixels, 10.2 x 10.2 mm imaging area	Back-illuminated 1024 x 1024 eXcelon3 EMCCD, 13 x 13 µm pixels, 13.3 x 13.3 mm imaging area
Shutter	25 mm shutter included	25 mm shutter included
ADC Speed	5, 10, 20, 30 & 36.67 MHz (EM mode)	5, 10, 20, & 30 MHz (EM mode) 1 MHz & 100 KHz (Normal CCD mode)
Read noise - **EM mode** (e^- rms) ** Effective read noise with on chip multiplication gain enabled.*	5 MHz 20 e^- (< 1 e^-)* 10 MHz 26 e^- (< 1 e^-)* 20 MHz 40 e^- (< 1 e^-)* 30 MHz 80 e^- (< 1 e^-)*	5 MHz 30 e^- (< 1 e^-)* 10 MHz 40 e^- (< 1 e^-)* 20 MHz 80 e^- (< 1 e^-)* 30 MHz 130 e^- (< 1 e^-)*
Read noise - **Normal CCD mode** (e^- rms)	*n/a*	100 KHz 3.5 e^- 1 MHz 4.0 e^-
Frame Rate	30 fps at 1Kx1K; >4,800 fps @ High Speed mode; >119,000 sps Spectra-Kinetics mode	25 fps at 1Kx1K; >4,800 fps @ High Speed mode; >300,000 sps Spectra-Kinetics mode
Linear full well - EM mode only	>150 ke- (output amplifier)	>500 ke- (output amplifier)
Linear full well EM and normal CCD modes	30 ke- (single pixel)	80 ke- (single pixel)
Deepest cooling temperature*	-70°C +/- 0.05°C @ +20°C ambient; 5 MHz ADC	-55°C +/- 0.05°C (guaranteed) @ +20°C ambient; 10MHz ADC Maximum Cooling: -65°C (air), -65°C (+20°C liquid)
Dark current	0.002 e^-/p/sec (typical) @ -70°C	0.002 e-/p/sec (typical), 0.04 e-/p/sec (maximum) @ -55°C
Vertical shift rate	800 nsec/row (variable)	700 nsec/row - 5 µsec/row (variable)

Clock induced charge (CIC) *Measured at 1000x EM Gain*	0.02 e^-/pixel/frame
Electron multiplication (EM) gain	1 to 1000x, controlled in linear, absolute steps
Trigger modes	External Trigger, Bulb Mode, Shift per Trigger, Single Trigger
I/O signals	Exposure, Readout, Trigger In, Image Shift, Waiting for Trigger
Operating environment	0 to 30°C ambient, 0 to 80% relative humidity, non-condensing
Certification	CE
Dimensions / Weight	8.02 inches (20.37 cm) x 6.79 inches (17.24 cm) x 5.8 inches (14.73 cm) L x W x H Approximately 9.2 lbs (4.2 kg)

* Due to increased thermal dissipation, a higher sensor temperature control point must be set at 36.67 MHz and 30 MHz or in high speed readout modes.
NOTE: All specifications are typical and are subject to change without notice.

ProEM-HS:1024BX3 & ProEM: 1KBX3-10um Rev. P4 *Page 3 of 11*

Teledyne Princeton Instruments | Main Office- (USA) | Tel: +1 609.587.9797 | pi.info@teledyne.com

Figure A.2. **Data Sheet, Page 3.**

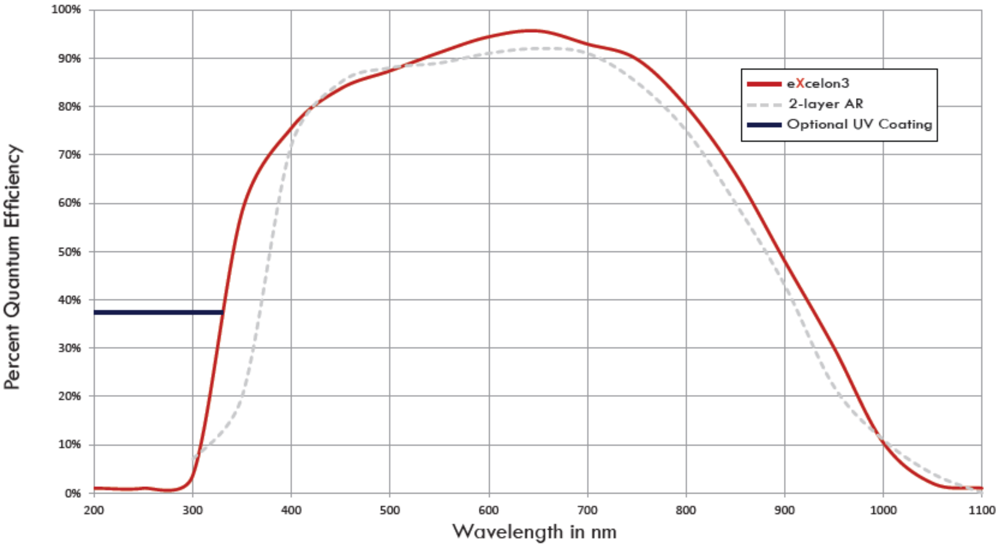

NOTE: Graph shows typical Quantum Efficiency (QE) data measured at + 25° C. Quantum Efficiency is a function of temperature and actual results will depend upon CCD temperature.

Figure A.3. **Quantum Efficiency.**

A.1.2 Specification Sheet

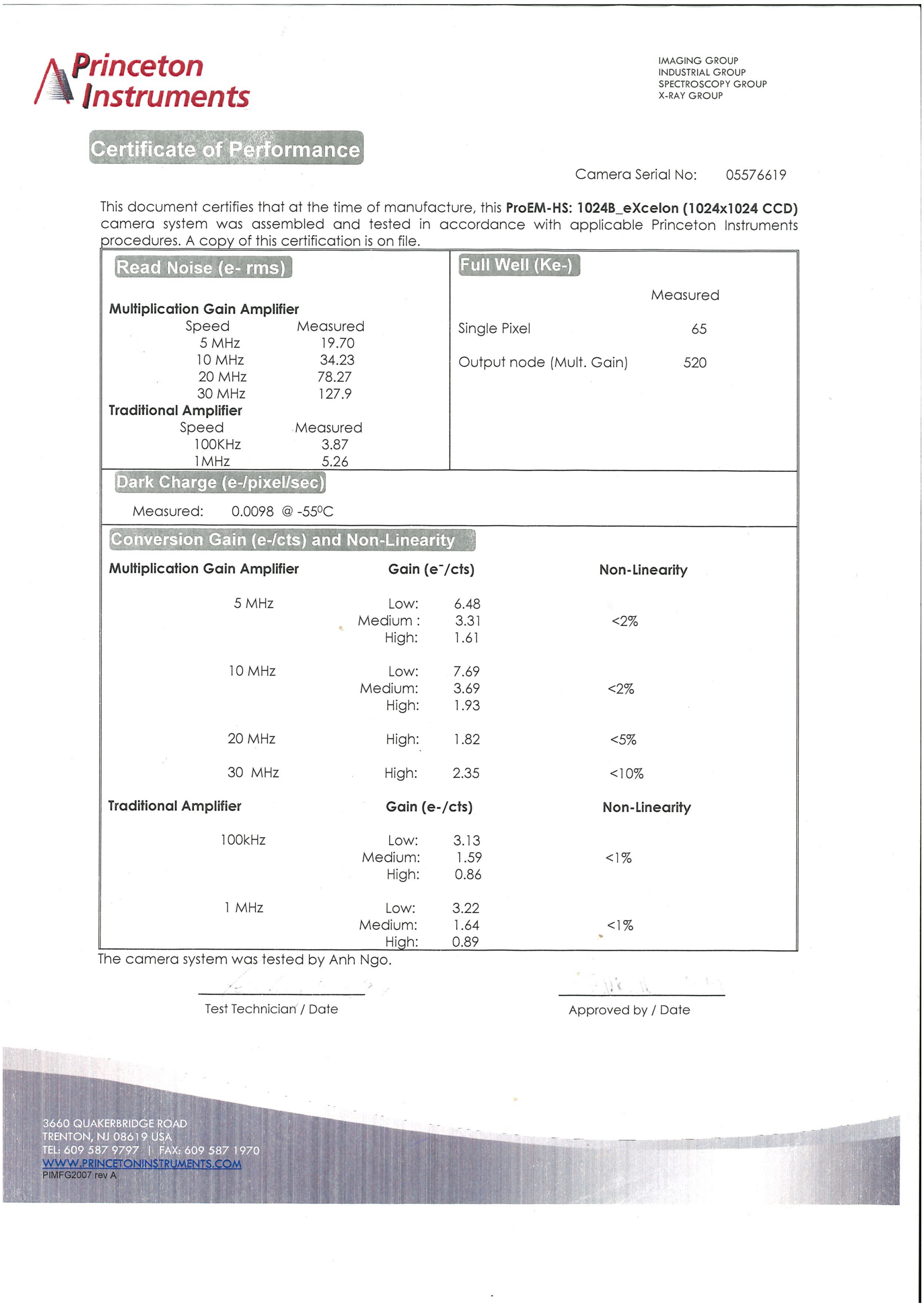

Princeton Instruments

IMAGING GROUP
INDUSTRIAL GROUP
SPECTROSCOPY GROUP
X-RAY GROUP

Certificate of Performance

Camera Serial No: 05576619

This document certifies that at the time of manufacture, this **ProEM-HS: 1024B_eXcelon (1024x1024 CCD)** camera system was assembled and tested in accordance with applicable Princeton Instruments procedures. A copy of this certification is on file.

Read Noise (e- rms)

Multiplication Gain Amplifier

Speed	Measured
5 MHz	19.70
10 MHz	34.23
20 MHz	78.27
30 MHz	127.9

Traditional Amplifier

Speed	Measured
100KHz	3.87
1MHz	5.26

Full Well (Ke-)

	Measured
Single Pixel	65
Output node (Mult. Gain)	520

Dark Charge (e-/pixel/sec)

Measured: 0.0098 @ -55°C

Conversion Gain (e-/cts) and Non-Linearity

Multiplication Gain Amplifier		**Gain (e⁻/cts)**	**Non-Linearity**
5 MHz	Low:	6.48	
	Medium :	3.31	<2%
	High:	1.61	
10 MHz	Low:	7.69	
	Medium:	3.69	<2%
	High:	1.93	
20 MHz	High:	1.82	<5%
30 MHz	High:	2.35	<10%
Traditional Amplifier		**Gain (e-/cts)**	**Non-Linearity**
100kHz	Low:	3.13	
	Medium:	1.59	<1%
	High:	0.86	
1 MHz	Low:	3.22	
	Medium:	1.64	<1%
	High:	0.89	

The camera system was tested by Anh Ngo.

Test Technician / Date

Approved by / Date

3660 QUAKERBRIDGE ROAD
TRENTON, NJ 08619 USA
TEL: 609 587 9797 | FAX: 609 587 1970
WWW.PRINCETONINSTRUMENTS.COM
PIMFG2007 rev A

Figure A.4. **Certificate of Performance for our Camera.**

A.1.3 Influence of Vertical Shift Speed on CICs

The creation of CICs is minimized by the camera's manufacturer by choosing the best amplitudes and shapes for the clock-voltages. The only parameter that can be controlled by the user via the camera's software is the vertical shift speed (VSS), which is given in μs. The VSS is the time it takes to vertically shift the frame on the CCD chip by one row towards the readout register. Shorter VSS times correspond to faster speeds. This of course also influences the readout time and thus the accessible frame rates. If the VSS is chosen too fast the charge transfer efficiency is reduced, and not all charges on a pixel are shifted correctly but some remain on the initial row. This is especially relevant in high-signal conditions. In theory, faster VSS are also expected to create less CICs [40]. In order to reduce spurious charges it is therefore recommended to choose the fastest VSS possible that still completely transfers all electrons.

This influence of the VSS on spurious charges was measured on our camera with the shutter closed and the usual camera settings ($g = 310$, $T = -65\,°$). The result can be seen in fig. A.5. Images were taken with different VSS settings and the average number of CICs per row extracted. The CCD chip is read out towards the left.

In the first ≈ 100 rows particularly many CICs are created, almost independently of the VSS. From row 100 to the end of the chip, the amount of CICs steadily increases. The fastest shift speed, $0.7\,\mu$s, shows slightly less spurious charges than $1.2\,\mu$s and $2\,\mu$s. A VSS of $5\,\mu$s produces noticeably more spurious charges. However, this effect is partly caused by the fact that the readout of the chip takes much longer, which gives thermal charges more time to accumulate. Overall, the influence of the VSS is not as great as measured in [39] for another camera that is based on the same EM CCD chip.

For the measurements in this thesis, a VSS of $0.7\,\mu$s was used.

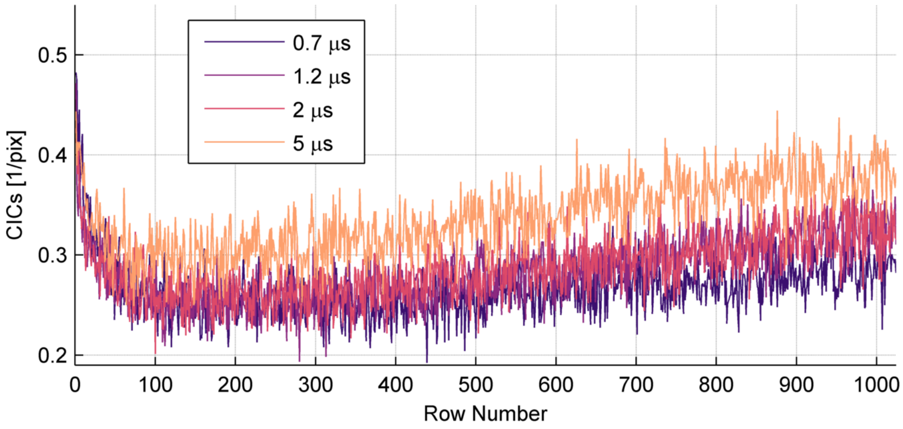

FIGURE A.5. **Influence of the VSS on the Creation of CICs.** Theoretically, a faster VSS should produce less CICs.

Bibliography

[1] S. Flörchinger, T. Haas, Á. Parra-López, N. Sánchez-Kuntz, and M. Tolosa-Simeón. “Scalar Quantum Fields in Cosmologies with 2+1 Spacetime Dimensions”. In: (2022). In preparation.

[2] L. Parker. “Quantized Fields and Particle Creation in Expanding Universes”. In: *Physical Review* 183 (1057 1969).

[3] J. Berges, A. Rothkopf, and J. Schmidt. “Nonthermal Fixed Points: Effective Weak Coupling for Strongly Correlated Systems Far from Equilibrium”. In: *Physical Review Letters* 101.041603 (2008).

[4] C.-M. Schmied, A. N. Mikheev, and T. Gasenzer. “Non-Thermal Fixed Points: Universal Dynamics far from Equilibrium”. In: *International Journal of Modern Physics A* 34.29 (2019), p. 1941006.

[5] R. Micha and I. I. Tkachev. “Turbulent Thermalization”. In: *Physical Review D* 70 (4 2004), p. 043538.

[6] J. Eisert, M. Freisdorf, and C. Gogolin. “Quantum Many-Body Systems out of Equilibrium”. In: *Nature Physics* 11 (2 2015), pp. 124–130.

[7] S. Flörchinger, T. Haas, M. Hans, E. Kath, N. Liebster, M. Oberthaler, Á. Parra-López, N. Sánchez-Kuntz, M. Sparn, H. Strobel, M. Tolosa-Simeón, and C. Viermann. “Curved and Expanding Space-Time Geometries in Bose-Einstein Condensates”. In: (2022). In preparation.

[8] B. Nowak, D. Sexty, and T. Gasenzer. “Superfluid Turbulence: Nonthermal Fixed Point in an Ultracold Bose Gas”. In: *Physical Review B* 84 (2 2011), p. 020506.

[9] M. Prüfer, P. Kunkel, H. Strobel, S. Lannig, D. Linnemann, C.-M. Schmied, J. Berges, T. Gasenzer, and M. K. Oberthaler. “Observation of Universal Dynamics in a Spinor Bose Gas far from Equilibrium”. In: *Nature* 563 (2018), pp. 217–220.

[10] V. A. Yurovsky, B. A. Malomed, R. G. Hulet, and M. Olshanii. “Dissociation of One-Dimensional Matter Wave Breathers due to Quantum Many-Body Effects”. In: *Physical Review Letters* 119 (22 2017), p. 220401.

[11] K. Staliunas, S. Longhi, and G. J. de Valcárcel. “Farraday Patterns in Bose-Einstein Condensates”. In: *Physical Review Letters* 89 (21 2002), p. 210406.

[12] L. W. Clark, A. Gaj, L. Feng, and C. Chin. “Collective Emission of Matter-Wave Jets from Driven Bose-Einstein Condensates”. In: *Nature* 551 (7680 2017), pp. 356–359.

[13] C. D’Errico, M. Zaccanti, M. Fattori, G. R. und M. Ingulscio, G. Modugno, and A. Simoni. “Feshbach Resonances in Ultracold ^{39}K”. In: *New Journal of Physics* 9.7 (2007), pp. 223–223.

[14] A. Chatrchyan, K. T. Geier, M. K. Oberthaler, J. Berges, and P. Hauke. "Analog Cosmological Reheating in an Ultracold Bose Gas". In: *Physical Review A* 104 (2 2021), p. 023302.

[15] P. A. Murthy, D. Kedar, T. Lompe, M. Neidig, M. G. Ries, A. N. Wenz, G. Zürn, and S. Jochim. "Matter-Wave Fourier Optics with a Strongly Interacting Two-Dimensional Fermi Gas". In: *Physical Review A* 90 (4 2014), p. 043611.

[16] W. S. Bakr, J. I. Gillen, A. Peng, S. Fölling, and M. Greiner. "A Quantum Gas Microscope for Detecting Single Atoms in a Hubbard-Regime Optical Lattice". In: *Nature* 462 (2009), pp. 74–77.

[17] L. W. Cheuk, M. A. Nichols, M. Okan, T. G. adnd V. V. Ramasesh, W. S. bakr, T. Lompe, and M. W. Zwierlein. "Quantum-Gas Microscope for Fermionic Atoms". In: *Physical Review Letters* 114 (19 2015), p. 193001.

[18] B. J. Lester, A. M. Kaufman, and C. A. Regal. "Raman Cooling Imaging: Detecting Single Atoms Near Their Ground State of Motion". In: *Physical Review A* 90 (1 2014), p. 011804.

[19] C. Chin, R. Grimm, P. Julienne, and E. Tiesinga. "Feshbach Resonances in Ultracold Gases". In: *Reviews of Modern Physics* 82.1225 (2010).

[20] A. J. Moerdijk, B. J. Verhaar, and A. Axelsson. "Resonances in Ultracold Collisions of ^{6}Li, ^{7}Li and ^{2}3Na". In: *Physical Review A* 51.4852 (1995).

[21] T. G. Tiecke. "Feshbach Resonances in Ultracold Mixtures of the Fermionic Quantum Gases ^{6}Li and ^{40}K". PhD Thesis. University of Amsterdam, 2009.

[22] M. Hans, F. Schmutte, C. Viermann, N. Liebster, M. Sparn, M. K. Oberthaler, and H. Strobel. "High Signal to Noise Absorption Imaging of Alkali Atoms at Moderate Magnetic Fields". In: *Review of Scientific Instruments* 92.023203 (2021).

[23] C. J. Foot. *Atomic Physics*. 2014th ed. Oxford, UK: Oxford University Press, 2005.

[24] D. P. DeMille, D. Budker, and D. F. Kimball. *Atomic Physics: An Exploration Through Problems and Solutions.* Oxford, UK: Oxford University Press, 2010.

[25] A. G. Badsen, C. A. Haniff, and C. D. Mackay. "Photon Counting Strategies with Low-Light-Level CCDs". In: *Monthly Notices of the Royal Astronomical Society* 345 (3 2003), pp. 985–991.

[26] K. Matsuo, M. C. Teich, and B. E. A. Saleh. "Noise Properties and Time Response of the Staircase Avalanche Photodiode". In: *Journal of Lightwave Technology* LT-3.6 (1985).

[27] M. Weidemüller, T. Esslinger, M. A. Ol'shanii, A. Hemmerich, and T. Hänsch. "A Novel Scheme for Efficient Cooling below the Photon Recoil Limit". In: *Europhysics Letters* 27.2 (1994), pp. 109–114.

[28] G. Salomon, L. Fouché, P. Wang, A. Aspect, P. Bouyer, and T. Bourdel. "Grey-Molasses Cooling of ^{39}K to a High Phase-Space Density". In: *Europhysics Letters* 104.6 (2013), p. 63002.

[29] C. Viermann. In preparation. PhD Thesis. University of Heidelberg, 2022.

[30] URL: `https://www.thorlabs.com/newgrouppage9.cfm?objectgroup_id=3313&pn=DMLP650L#8052`.

[31] URL: `https://www.semrock.com/filterdetails.aspx?id=ff01-766/13-25`.

[32] URL: `https://www.ahf.de/produkte/spektralanalytik-photonik/optische-filter/einzelfilter/laser-filter/emitter/notch-filter/2216/single-notch-filter-fuer-532-nm-zet532nf?c=187`.

[33] URL: `https://www.photometrics.com/learn/camera-test-protocol`.

[34] URL: `www.princetoninstruments.com/Uploads/Princeton/Documents/Whitepapers/onchipgain.pdf`.

[35] URL: `https://andor.oxinst.com/learning/view/article/electron-multiplying-ccd-cameras`.

[36] *ProEM HS:1024BX3 Datasheet.*
Teledyne Princeton Instruments. New Jersey, USA, 2020.

[37] URL: `https://andor.oxinst.com/learning/view/article/an-overview-of-em-gain-ageing-in-emccd-sensors`.

[38] A. Bergschneider, V. M. Klinkhammer, J. H. Becher, R. Klemt, G. Zürn, P. M. Preiss, and S. Jochim. “Spin-Resolved Single-Atom Imaging of ^{6}Li in Free Space”.
In: *Physical Review A* 97 (6 2018), p. 063613.

[39] J. H. W. Becher. “Towards Spin and Site-Resolved, Single Atom Imaging of ^{6}Li Atoms in a Multiwell Potential”. Master’s Thesis. University of Heidelberg, 2016.

[40] URL: `https://andor.oxinst.com/learning/view/article/ccd-system-considerations`.

Erklärung

Ich versichere, dass ich diese Arbeit selbstständig verfasst habe und keine anderen als die angegebenen Quellen und Hilfsmittel benutzt habe.

Heidelberg, den 23.02.2022 .... Elinor ....

Acknowledgments - Danksagung

On this last page of my thesis I will take the opportunity and thank everyone who made this thesis possible in the first place.

First of all, I want to thank Prof. Dr. Markus Oberthaler for the opportunity to do my Master's project in his research group. Your excitement for physics is definitely catching, and I am excited to continue as a PhD student under your supervision. Also I would like to thank Prof. Dr. Selim Jochim for acting as my second referee.

A huge THANK YOU goes to the BECK-team. I've learned a lot this last year. About physics, problem solving, and the BECK experiment (which I found intimidatingly complicated in the beginning and which I thought I'd never understand). I also learned to discuss the ingredients of store-bought food (in detail!) and to speculate how the packaging might be produced. I came to enjoy a grand selection of "special" chocolate flavours, realized that some people apparently need more salt than I do, and so much more. They say Teamwork Makes The Dream Work, and they are right. I am thrilled to be part of the team!

The Matterwave group as a whole is a wonderfully outgoing and welcoming bunch of rascals. Thank you for the readily offered help, no matter if I was looking for physics advice or life advice, the friendly working atmosphere and the strong team spirit.

Of course, all of this wouldn't have been possible without the love, support, life advice and Fresspäckchen from my parents and sister. Thank you for making sure that I never run out of olive oil, coffee, tea or spices, Tempos or socks. Your efforts are greatly appreciated!

I also want to thank my friends for keeping it real and always being there for each other. Each of you does life your own way, and I am honestly so proud of you. Grüße gehen raus an Alena, who makes sure that life doesn't get to vanilla and who just gets me.

Last, but definitely not least, I want to thank my longtime best friend and partner in crime, who excitedly channels my eccentric ideas, puts up with my stubbornness with (almost) endless patience and just takes me the way I am. @ "